White Rose Research Online

eprints@whiterose.ac.uk
https://eprints.whiterose.ac.uk
Universities of Leeds, Sheffield and York

Deposited via The University of York.

White Rose Research Online URL for this paper:
https://eprints.whiterose.ac.uk/id/eprint/247207/

Version: Published Version

Article:
Van Parys, G., Graves, J. P., Merle, A. et al. (2026) Investigation of finite aspect ratio effects in axisymmetric magnetic equilibria with toroidal rotation and pressure anisotropy. Plasma Physics and Controlled Fusion. 075003. ISSN: 1361-6587

https://doi.org/10.1088/1361-6587/ae8058

Reuse
This article is distributed under the terms of the Creative Commons Attribution (CC BY) licence. This licence allows you to distribute, remix, tweak, and build upon the work, even commercially, as long as you credit the authors for the original work. More information and the full terms of the licence here: https://creativecommons.org/licenses/

Takedown
If you consider content in White Rose Research Online to be in breach of UK law, please notify us by emailing eprints@whiterose.ac.uk including the URL of the record and the reason for the withdrawal request.

UNIVERSITY OF LEEDS
University of Sheffield
UNIVERSITY of York

Plasma Physics and
Controlled Fusion

PURPOSE-LED
PUBLISHING™

PAPER • OPEN ACCESS

Investigation of finite aspect ratio effects in axisymmetric magnetic equilibria with toroidal rotation and pressure anisotropy

To cite this article: G Van Parys *et al* 2026 *Plasma Phys. Control. Fusion* **68** 075003

View the article online for updates and enhancements.

You may also like

- TORQSNet: a physics-inspired spectral neural network for predicting toroidal torque density in tokamak devices
Hanyu Zhang, Yueqiang Liu, Xu Yang et al.
- Simulation design for subluminal velocity-controlled spatio-temporal drivers in laser–plasma wakefields
Chiara Badiali, Rafael Almeida, Thales Silva et al.
- Attosecond electron bunch generation by an intense high-order harmonic pulse interacting with a thin target
Yang He, Cheng-Qi Zhang, Mamat Ali Bake et al.

This content was downloaded from IP address 144.32.240.131 on 26/10/2026 at 12:11

Plasma Physics and Controlled Fusion

Check for updates

OPEN ACCESS

RECEIVED
12 February 2026

REVISED
13 May 2026

ACCEPTED FOR PUBLICATION
22 June 2026

PUBLISHED
2 July 2026

Original content from this work may be used under the terms of the Creative Commons Attribution 4.0 licence.

Any further distribution of this work must maintain attribution to the author(s) and the title of the work, journal citation and DOI.



PAPER

Investigation of finite aspect ratio effects in axisymmetric magnetic equilibria with toroidal rotation and pressure anisotropy

G Van Parys[1,*], J P Graves[1,2], A Merle[1], C Heiss[1], M Bassanini[1] and T Glauser[1]

[1] École Polytechnique Fédérale de Lausanne, Swiss Plasma Center, CH-1015 Lausanne, Switzerland
[2] York Plasma Institute, Department of Physics, University of York, Heslington, York YO10 5DD, United Kingdom
[*] Author to whom any correspondence should be addressed.

E-mail: guillaume.vanparys@epfl.ch

Keywords: MagnetoHydrodynamics, magnetic equilibrium, pressure anisotropy, rotation

Abstract

The inverse equilibrium formulation and numerical code described in (Lao L L 1981 *Phys. Fluids* **24** 1431–40) are extended in a new 'exact' fixed boundary equilibrium code that accounts for plasma toroidal rotation and pressure anisotropy. The formulation precisely captures deviations from an inverse aspect ratio $\epsilon := a/R_0$ expansion, at various orders, with a a minor radius and R_0 the major radius at the magnetic axis. We show that for experimentally relevant elongation $\kappa \lesssim 2$ and moderate aspect ratio $\epsilon \sim 0.3$, next to leading order (NLO) effects driven mainly by elongation and triangularity are important especially for the Shafranov shift. For the plasma diamagnetism, order unity deviations are seen at moderate pressures, even though the NLO contribution is weak. The impact of strong perpendicular anisotropy on shaping is investigated, as it was theoretically proposed in (Madden and Hastie 1994 *Nucl. Fusion* **34** 519) that temperature ratios such that $\epsilon T_\perp/T_\parallel \sim 1$ would lead to leading order modifications of the shaping through the strong poloidal localization of the perpendicular pressure. We show through a near-axis analysis that the leading order distribution function must be chosen carefully for consistency, and we verify numerically that shaping modifications due to the anisotropy or rotation remain small for conventional poloidal betas $\beta_p \sim 1$.

1. Introduction & motivation

Reliable magnetic equilibrium descriptions lie at the base of nearly every calculation in tokamak physics: stability thresholds, particle orbits, and neoclassical and turbulent transport all depend on an accurate description of the magnetic equilibrium geometry. In the most familiar formulation the axisymmetric force balance is written as an elliptic equation for the poloidal flux; alternatively, the inverse formulation solves instead directly for the parametrization of the flux surfaces. That viewpoint enables the powerful asymptotic expansion in inverse aspect ratio (Greene *et al* 1971, Connor and Hastie 1985, Fitzpatrick 2024), where effects due to toroidicity are treated as perturbations, and semi-analytical results are achievable for any form of pressure profile and current distribution, unlike Solov'ev type solutions which are restricted to non-vanishing current densities at the edge. Additional physics such as toroidal rotation and pressure anisotropy can straightforwardly be included in the expansion (Madden and Hastie 1994), enabling to take those into account analytically in orbit studies and in MHD-stability problems (Graves 2004, Jucker *et al* 2008). These two effects arise in discharges with auxiliary heating such as ICRH with minority heating leading to strong perpendicular anisotropy, or tangential NBI leading to parallel anisotropy and mass flows that can become sonic for Spherical Tokamaks (ST). Since conventional aspect ratio Tokamaks and STs have their aspect ratio such that $\epsilon \approx 0.3 - 0.5$ or higher, leading order results may not accurately reflect the equilibrium geometry.

In this article, we quantitatively analyze the deviations from the $\epsilon-$expansion for experimentally relevant parameters, taking into account both rotation and anisotropy via a kinetic closure. This is done

© 2026 The Author(s). Published by IOP Publishing Ltd

by keeping the inverse aspect ratio ϵ as an input parameter by appropriately normalizing the underlying equations, allowing scans that verify the error scaling with ϵ. Numerically we discretize the minor radial force balance residuals with B-spline finite elements (FEs) and solve the resulting nonlinear system with a Newton method, having obtained the residuals and the analytical Jacobian using a computer algebra system (CAS). The approach allows calculation of exact fixed boundary equilibria, and its comparison with an inverse aspect ratio expansion at user-defined order. Although several numerical implementations now solve rotating and anisotropic equilibria self-consistently (see e.g. Cooper *et al* (2009) for 3D equilibria, (Guazzotto *et al* 2004) for poloidal and toroidal flows, (Fitzgerald *et al* 2013) for free-boundary equilibrium reconstruction), the foundational theory already showed that flow and anisotropy displace pressure and density contours away from flux surfaces and affect the Shafranov Shift via an effective dynamic pressure $p_{\|} + p_{\perp} + (1/2)\rho u^2$. In particular, (Iacono *et al* 1990) derived axisymmetric equilibria with general flows and anisotropic pressure, obtaining expressions for the density shift for specific closures, and for the Shafranov shift for a rotating bi-Maxwellian, in the large aspect ratio expansion. On the other hand, (Madden and Hastie 1994) treated the strongly perpendicular anisotropic case $\epsilon T_{\perp}/T_{\|} \sim 1$ in that same expansion, and found that non-circular shaping enters at lower order than previously appreciated. For the contour shifts discussed above, the leading effect can be captured by an effective dynamic pressure, and in that sense the problem may be treated perturbatively once the geometry is known (i.e. solve an effective isotropic-static equilibrium problem, then evaluate the equations of state on the obtained fields). The predictions of Madden and Hastie (1994) are different: their asymptotic calculation predicts a genuinely self-consistent correction to shaping. Motivated by these asymptotic studies, we investigate numerically whether the equilibrium solutions converge to the expected inverse-aspect-ratio ordering, and we derive the higher-order shaping corrections that emerge within our self-consistent formulation. The asymptotic expansion is thus the natural framework for isolating this kind of physical effect and, in the present work, for checking whether the numerical equilibria converge toward the asymptotic prediction at the order expected from the theory. To our knowledge, such an order-by-order convergence test against aspect ratio has not previously been demonstrated, even for the simplest, isotropic-static case. A further advantage of our formulation is that, unlike existing equilibrium codes, it combines the full rotating-anisotropic physics with the geometrical formulation of the equilibrium problem, in the same coordinates used in analytical MHD stability theory and in drift-precession studies (e.g. Jucker *et al* (2008), Graves (2013)). At present, the consistent theoretical investigation of pressure-driven instabilities with arbitrary pressure anisotropy (from $T_{\perp}/T_{\|} \sim 1$ to $T_{\perp}/T_{\|} \gg 1$) remains an open problem: no analytic stability theory correctly accounts for anisotropy in the equilibrium for such modes, extending the classic internal-kink framework of Bussac *et al* (1975) and the natural shaping corrections of Wahlberg (2004). The equilibrium expansions derived here, together with their numerical verification, establish the self-consistent geometric basis that such a theory will require, as will be demonstrated in future work. The paper is organized as follows. The governing equations are presented in section 2 with the chosen coordinates and flux surface parametrization. This is followed in section 2.1 by the normalization of the equations, and in section 2.2 by the adopted kinetic closure and distribution function models adopted in the numerical examples. The details of the numerical discretization via finite-elements are shown in section 2.3. Next, the analytical results leveraging the inverse aspect ratio expansion are presented in section 3, which contains the general setting 3.1, LO predictions in section 3.2, and novel next to leading order (NLO) predictions in section 3.3. The numerical results follow in section 4 and we conclude the work in section 5.

2. Problem formulation

We start from the flowing, anisotropic pressure force balance:

$$\boldsymbol{F} = \rho(\boldsymbol{u}\cdot\nabla)\boldsymbol{u} + \nabla\cdot\mathbb{P} - \boldsymbol{j}\times\boldsymbol{B} \equiv 0 \tag{2.1}$$

Assuming axisymmetry $\partial_\phi \equiv 0$, the magnetic field is conveniently represented by $\boldsymbol{B} = \nabla\phi\times\nabla\psi + RB_\phi\nabla\phi$. We take into account only leading order flows in an axisymmetric magnetized plasma which are species independent and can be shown to be of the form $\boldsymbol{u} = R^2\Omega(\psi)\nabla\phi$ (Abel *et al* 2013). The pressure tensor is at this same order of the CGL form: $\mathbb{P} = p_{\perp}\mathbb{I} + (p_{\|} - p_{\perp})\boldsymbol{bb}$ where $\boldsymbol{b}$ is the unit vector parallel to the local magnetic field, $\boldsymbol{bb}$ denotes its dyadic product. We use lowercase $(\rho, p_{\|}, p_{\perp})$ for Eulerian fields (functions on the poloidal plane), while uppercase $(\varrho, P_{\|}, P_{\perp})$ denote the constitutive state functions of the parameter triple (ψ, R, B). These constitutive relations are obtained assuming that all species have

distribution functions that depend on the following constants of motion:

$$\mathcal{E} = \frac{1}{2} m w_{\parallel}^2 + \mu B + q\Phi_1 - \frac{1}{2} m \boldsymbol{u}^2, \quad \mu = \frac{w_{\perp}^2}{2B}, \quad \frac{P_\phi}{Ze} \approx \psi \tag{2.2}$$

where $(w_{\parallel}, w_{\perp})$ denote respectively the parallel and perpendicular velocities of the particle in the frame rotating with $\boldsymbol{u}$. Also, Φ_1 is the first order electrostatic potential ensuring quasineutrality. Note that $\Omega = -\partial\Phi_0/\partial\psi$ is related to the leading order $\boldsymbol{E}\times\boldsymbol{B}$ drift. Assuming that ψ is the conserved quantity neglects finite orbit width effects. The energy-like variable $\mathcal{E}$ is obtained by a combination of constants of motion $\mathcal{E} = E - q\Phi_0(\psi^*)$ with $\psi^* = P_\phi/Ze$ and $E = \frac{1}{2} m(\boldsymbol{u} + w_{\parallel}\boldsymbol{b})^2 + \mu B + q(\Phi_0 + \Phi_1)$ is the particle energy in the laboratory frame. Taking the scalar product of equation (2.1) with $\nabla\phi$ leads to:

$$\left(1 - \sigma_{\parallel}\right) R B_\phi = T(\psi) \tag{2.3}$$

with $\sigma_{\parallel} = \mu_0(p_{\parallel} - p_{\perp})/B^2$ and T an arbitrary function of the poloidal flux. The parallel force balance is identically satisfied provided the maps $(\varrho, P_{\parallel}, P_{\perp})$ satisfy the conditions described above. We now choose independent coordinates (r,ω,ϕ), such that $\psi = \psi(r)$. ω is for now a generic poloidal angle, which will be fixed by the choice of parametrization $(R(r,\omega), Z(r,\omega))$ in equation (2.5) and it is shown in appendix E.2 how to construct such coordinates from an arbitrary flux map. We define the following geometrical quantities:

$$J = R\left[\left(\partial_r R\right)\left(\partial_\omega Z\right) - \left(\partial_\omega R\right)\left(\partial_r Z\right)\right]$$

and

$$g_{\omega\omega} = \left(\partial_\omega R\right)^2 + \left(\partial_\omega Z\right)^2, \quad g_{r\omega} = \left[\left(\partial_r R\right)\left(\partial_\omega Z\right) + \left(\partial_\omega R\right)\left(\partial_r Z\right)\right].$$

In the anisotropic case, the constitutive relations involve non trivially the magnetic field strength B, i.e. explicitly, the pressures and the density are related via: $p_{\parallel}(r,\omega) = P_{\parallel}[\psi(r), R(r,\omega), B(r,\omega)]$ and similarly for $p_{\perp}$ and ρ. We thus rewrite (2.3) as an equation determining B:

$$B^2 = \psi'^2 \frac{g_{\omega\omega}}{J^2} + \frac{1}{\left(1-\sigma_{\parallel}\right)^2}\frac{T^2}{R^2}$$

where the RHS depends on B through $\sigma_{\parallel}$. Finally, we obtain the generalized Grad-Shafranov equation from the covariant component of the force in (2.1) $\boldsymbol{F}\cdot\boldsymbol{e}_\psi$:

$$\begin{aligned} F_\psi = {} & \frac{\psi'}{JR}\left[\frac{\partial}{\partial r}\left(\frac{\psi' g_{\omega\omega}}{JR}\right) - \frac{\partial}{\partial\omega}\left(\frac{\psi' g_{r\omega}}{JR}\right)\right] + \frac{(RB_\phi)}{R^2}\frac{\partial(RB_\phi)}{\partial r} + \frac{\partial p_\perp}{\partial r} \\ & - \frac{\psi'^2}{2J^3}\left(2 g_{r\omega}\sigma_{\parallel}\frac{\partial J}{\partial\omega} - J\left[2 g_{r\omega}\frac{\partial\sigma_{\parallel}}{\partial\omega} + \sigma_{\parallel}\left(2\frac{\partial g_{r\omega}}{\partial\omega} + \frac{\partial g_{\omega\omega}}{\partial r}\right)\right]\right) - \sigma_{\parallel}\frac{(RB_\phi)^2}{R^3}\frac{\partial R}{\partial r} \\ & - \rho R\Omega^2\frac{\partial R}{\partial r}. \end{aligned} \tag{2.4}$$

The first line corresponds to the usual isotropic static MHD force balance with replacements $p_{\perp} \to p(r)$ and $RB_\phi \to F(r)$ At this point, we set the reparametrization freedom assuming up-down symmetric flux surfaces for simplicity (Madden and Hastie 1994, Graves 2013):

$$\begin{aligned} R(r,\omega) &= R_0 + r\cos\omega - \Delta(r) + \sum_{k\geqslant 2} S_k(r)\cos\left[(k-1)\omega\right] + P(r)\cos\omega \\ Z(r,\omega) &= r\sin\omega - \sum_{k\geqslant 2} S_k(r)\sin\left[(k-1)\omega\right] + P(r)\sin\omega \end{aligned} \tag{2.5}$$

R_0 is assumed to be the magnetic axis, i.e. $\Delta(0) = 0$, S_2 sets the elongation, S_3 the triangularity and so on. The profile $P(r)$ is introduced to set the following Jacobian gauge (Graves 2013):

$$\frac{r}{R_0} = \frac{1}{2\pi}\int_0^{2\pi} \mathrm{d}\omega \frac{J}{R^2} \tag{2.6}$$

which, in combination to the following relation for the poloidal flux:

$$\psi'(r) = \frac{r}{R_0}\frac{T(r)}{q(r)}$$

allows to use the same radial coordinate r as in the straight field line system with angular coordinate $\vartheta = \vartheta(r,\omega)$ and its Jacobian $J_\vartheta = \left[\nabla r \cdot (\nabla\vartheta \times \nabla\phi)\right]^{-1} = rR^2/R_0$. Here $q(r)$ is the safety factor which we treat as a given input. This means that $T(r)$ must be solved for by enforcing the flux-surface averaged momentum balance: $\langle JF_\psi \rangle = 0$, where $\langle\cdot\rangle := (2\pi)^{-1}\int_0^{2\pi} \mathrm{d}\omega$. This is a first order non-linear differential equation for T, and its boundary condition can be chosen to be $T(0) = (1-\sigma_{\parallel,0})^{-1} R_0 B_0$ fixing the axis magnetic field strength, with $\sigma_{\parallel,0} = \sigma_\parallel(\hat{r}=0,\omega)$. The shaping profiles $(\Delta, S_{k\geqslant 2})$ are determined by the Fourier harmonics of the flux-averaged force balance,

$$\langle \cos(k\omega)\, \hat{J} F_\psi \rangle = 0. \tag{2.7}$$

Equations (2.7) are much simpler than the Euler–Lagrange (EL) moment equations obtained from the static isotropic variational principle presented in Lao *et al* (1981) and explicited for our coordinates and parametrization in appendix A. Numerical tests show that using the Fourier form (2.7) reproduces the EL results while offering the practical advantage of evaluating the residuals efficiently via an FFT and considerably simplifying the Jacobian assembly. For the boundary conditions: at the axis, single-valuedness in ω forces $S_k(0) = 0$, while the definition of the magnetic axis being R_0 leads to $\Delta(0) = P(0) = 0$. This is unlike in Lao *et al* (1981), where a profile $R_0(r)$ is solved for with fixed outer boundary condition, so that finding $R_0(0)$ is part of the problem. We choose to replace this outer boundary condition by fixing *a priori* the aspect ratio $A = R_0/a$ where $r = a$ denotes the plasma-vacuum boundary. For the other harmonics S_k, a boundary condition at the plasma-vacuum interface must be provided, this means setting fixed values for $S_k(a)$ for $k \geqslant 2$. This concludes the set of equations that we solve: given the safety factor $q(r)$, the constitutive relations $(\varrho, P_\parallel, P_\perp)$ i.e. their functional dependence in (r,R,B), and the boundary values $S_k(a)$, we solve for the profiles $\{T, \Delta, S_k, P\}$ and the field $B(r,\omega)$.

2.1. Normalization

In this section we normalize the quantities appearing in the previous section, putting the equations in a form suitable to be expanded in $\epsilon := a/R_0$. As in Fitzpatrick (2024), we introduce the following:

$$\hat{R} = \frac{R}{R_0}, \quad \hat{Z} = \frac{Z}{R_0}, \quad \hat{r} = \frac{r}{a}, \quad \hat{\Delta} = \frac{\Delta}{\epsilon a}, \quad \hat{S}_n = \frac{S_n}{\epsilon a}, \quad \hat{P} = \frac{P}{\epsilon^2 a}, \quad \hat{B} = \frac{B}{B_0}.$$

Leading to the expressions:

$$\begin{aligned}
\hat{R}(\hat{r},\omega) &= 1 + \epsilon\hat{r}\cos\omega - \epsilon^2\hat{\Delta}(r) + \epsilon^2 \sum_{k\geqslant 2} \hat{S}_k(\hat{r}) \cos\left[(k-1)\omega\right] + \epsilon^3 \hat{P}(\hat{r}) \cos\omega \\
\hat{Z}(\hat{r},\omega) &= \epsilon\hat{r}\sin\omega - \epsilon^2 \sum_{k\geqslant 2} \hat{S}_k(\hat{r}) \sin\left[(k-1)\omega\right] + \epsilon^3 \hat{P}(\hat{r}) \sin\omega
\end{aligned} \tag{2.8}$$

and also define pressure-related normalized quantities:

$$\bar{\beta}_{t0} = \frac{\mu_0}{B_0^2}\frac{p_\parallel + p_\perp}{2}, \quad \hat{\sigma}_\parallel = \frac{\beta_{t\parallel} - \beta_{t\perp}}{\hat{B}^2}, \quad \varrho\mathcal{M}^2 = \frac{\mu_0}{B_0^2}\rho R_0^2 \Omega^2. \tag{2.9}$$

The normalized magnetic field strength is Fourier expanded:

$$\hat{B}(\hat{r},\omega) = 1 + \epsilon \sum_{\ell\geqslant 0} \hat{B}_\ell(\hat{r}) \cos(\ell\omega) \tag{2.10}$$

and rewrite:

$$\hat{T} = \frac{T}{R_0 B_0} = 1 - \hat{\sigma}_{\parallel 0} + \epsilon^2 t_2(\hat{r}), \quad f(\hat{r}) = \frac{\psi'}{R_0 B_0} = \epsilon\hat{r}\frac{\hat{T}(\hat{r})}{q(\hat{r})}$$

where $f(\hat{r})$ represents the normalized poloidal magnetic field. We have introduced the profile t_2 which is related to the plasma toroidal diamagnetism, and $\hat{\sigma}_{\parallel,0}$ the normalized anisotropy parameter at the axis, introduced here so that the relevant boundary condition is $t_2(0) = 0$ enforcing B_0 to be the axis magnetic field. We denote by $\hat{J}, \hat{g}_{\omega\omega}$ and $\hat{g}_{\hat{r}\omega}$ the corresponding geometrical fields evaluated using $(\hat{R}, \hat{Z})$ and as functions of $\hat{r}$. The above definitions lead to the following equation for the square of the normalized magnetic field strength:

$$\hat{B}^2 = \epsilon^2 f^2 \frac{\hat{g}_{\omega\omega}}{\hat{J}^2} + \frac{1}{\left(1-\hat{\sigma}_\parallel\right)^2}\frac{\hat{T}^2}{\hat{R}^2} \tag{2.11}$$

which is used to solve for the Fourier amplitudes $\hat{B}_\ell$. We define $\widehat{RB_\phi} = \hat{T}/(1-\hat{\sigma}_\parallel)$, and express the normalized extended GSE from 2.4 as:

$$\begin{aligned}\hat{F}_\psi = \epsilon^2 \frac{f}{\hat{J}}\left[\frac{\partial}{\partial \hat{r}}\left(\frac{f\tilde{g}_{\omega\omega}}{\hat{J}}\right) - \frac{\partial}{\partial \omega}\left(\frac{f\tilde{g}_{\hat{r}\omega}}{\hat{J}}\right)\right] + \frac{\widehat{RB_\phi}}{\hat{R}^2}\frac{\partial \widehat{RB_\phi}}{\partial \hat{r}} + \frac{\partial \beta_{t\perp}}{\partial \hat{r}} \\ - \epsilon^2 \frac{f^2}{2\hat{J}^3}\left(2\hat{g}_{\hat{r}\omega}\hat{\sigma}_\parallel \frac{\partial \hat{J}}{\partial \omega} - \hat{J}\left[2\hat{g}_{\hat{r}\omega}\frac{\partial \hat{\sigma}_\parallel}{\partial \omega} + \hat{\sigma}_\parallel\left(2\frac{\partial \hat{g}_{\hat{r}\omega}}{\partial \omega} + \frac{\partial \hat{g}_{\omega\omega}}{\partial \hat{r}}\right)\right]\right) - \hat{\sigma}_\parallel \frac{\widehat{RB_\phi}^2}{\hat{R}^3}\frac{\partial \hat{R}}{\partial \hat{r}} \\ - \varrho \hat{R}\mathcal{M}^2 \frac{\partial \hat{R}}{\partial \hat{r}}.\end{aligned} \tag{2.12}$$

For the constitutive relations, a change in units of B being immaterial, we can assume that they are of the form $P_\parallel = P_\parallel(\hat{r}, \hat{R}, \hat{B})$, removing B_0 from the equations, while a and R_0 appear only through ϵ. We introduce the normalized constitutive relations

$$\Pi_{\parallel,\perp} := \mu_0 P_{\parallel,\perp}/B_0^2 \tag{2.13}$$

which will allow us to express the next section results independently of the choice of underlying distribution function. The last equation that we solve determines $\hat{P}(\hat{r})$ through:

$$\epsilon^2 \hat{r} = \frac{1}{2\pi}\int_0^{2\pi} \mathrm{d}\omega \frac{\hat{J}}{\hat{R}^2}. \tag{2.14}$$

The set of equations (2.11), (2.12) and (2.14) are what we solve in the next section via the asymptotic expansion, and in section 2.3 the full problem numerically. We remark in closing this section that for the numerical problem these normalizations amount to rescalings, and no assumption on the order of magnitude of the quantities introduced is made.

2.2. Kinetic closure

The equations presented above need to be closed by providing the functional dependence of $(\varrho, \Pi_\parallel, \Pi_\perp)$. For distributions functions that are functions of the constants of motion we have Grad (1967):

$$\Pi_\perp = \Pi_\parallel - \hat{B}\left(\frac{\partial \Pi_\parallel}{\partial \hat{B}}\right)_{\hat{r},\hat{R}}, \qquad \varrho \hat{R}\mathcal{M}^2 = \left(\frac{\partial \Pi_\parallel}{\partial \hat{R}}\right)_{\hat{r},\hat{B}} \tag{2.15}$$

which specifies all functions appearing in equation (2.12) provided the map $\Pi_\parallel$ is given. In this work, the approach taken is to model anisotropy and rotation with as few parameters as necessary to obtain their impact on the equilibrium problem, in contrast to a more detailed modeling which would for example separate ions, electrons, and a fast particle species, and treat quasineutrality self-consistently. We note that this is standard practice when studying this kind of physics in the equilibrium (as e.g. de Blank (1991), Madden and Hastie (1994), Fitzgerald *et al* (2013)) but it is inadequate for more precise equilibrium reconstruction applications. We detail in appendix F the splitting of the plasma kinetic functions into various species. The first form of anisotropic distribution function that we analyze is the so-called modified bi-Maxwellian that has been fully implemented in the VMEC and SCENIC workflow (Graves *et al* 2006):

$$\Pi_\parallel(\hat{r}, B) = \beta_0(\hat{r}) \begin{cases} \dfrac{B}{B_c}\dfrac{1 + A(1 - B/B_c) - 2\left[A(1-B/B_c)\right]^{5/2}}{1 - \left[A(1-B/B_c)\right]^2} & \text{if } B < B_c \\ \dfrac{B}{\left[A(r)B - (A(r)-1)B_c\right]} & \text{if } B \geqslant B_c \end{cases} \tag{2.16}$$

where we have omitted the hats because the formula above is invariant under a change of units as stated in section 2.1. B_c can in general be a profile, but we will specialize to the case of a constant B_c in what follows. Here $A = \hat{T}_\perp/T_\parallel$ is a measure of anisotropy, as defined in Graves *et al* (2006). The case analyzed in Madden and Hastie (1994), is obtained by taking $B_c(r) = \min_\omega \hat{B}(r,\omega)$ but a near axis expansion of the force balance presented in appendix C shows that this is an inconsistent choice. For the rotation with the anisotropy, we take a model distribution of fully parallel anisotropic population:

$$\mathcal{F}(\psi, \mathcal{E}, \mu) \propto \exp\left\{-\frac{\mathcal{E}}{T_\parallel(\psi)}\right\}\delta(\mu)$$

capturing the effects of rotation and of pressure anisotropy and can be seen as a limiting case for discharges with tangential NBI. This leads to the following expression for the parallel pressure:

$$\Pi_{\|}\left(\hat{r},\hat{R},\hat{B}\right)=\beta_0\left(\hat{r}\right)\exp\left(\mathcal{M}_0^2\left(\hat{r}\right)\hat{R}^2\right)\hat{B} \tag{2.17}$$

exhibiting the typical high-field-side (HFS) shift of the pressure due to the dominantly passing population (linear dependence in B) and the competing outward shift from the rotation. The isotropic case is obtained by simply removing the $\hat{B}$ prefactor. As shown in Graves and Wahlberg (2017), the above model can be appropriate to describe plasmas with $T_i \neq T_e$ and impurities provided the parameter $\mathcal{M}_0^2$ is suitably set.

2.3. Discretization & numerical implementation

Initially a straightforward adaptation of the method presented in Lao *et al* (1981) to cases with pressure anisotropy, rotation and with the use of the coordinates introduced in this work was attempted. It was soon realized that using a shooting method with an Initial Value Problem (IVP) solver would be impractical for the following reasons: radial derivatives of the magnetic field strength $\partial_{\hat{r}}\hat{B}$ are present in the generalized GSE (2.12), so with an IVP solver these would have to be computed via an implicit differentiation of the non-linear algebraic equation (2.11) determining $\hat{B}$, involving the highest order derivatives of the unknowns. The coordinates and parametrization used also lead to the same problem even in the standard static isotropic problem. Moreover, putting equation (2.7) into the canonical form $u'=f(x,u)$ requires significant symbolic manipulations. Solving the system of equations as a boundary-value problem allows direct access to the unknowns and their derivatives without unnecessary algebraic manipulations of the underlying equations. The main difficulty with the current approach is that in order to solve the resulting set of non-linear algebraic equations, one must provide the Jacobian of the residuals with respect to the unknowns or some approximation of its inverse for Jacobian-Free preconditioned methods. The Jacobian can be obtained symbolically with CAS. Using equation (2.7) instead of the EL equations presented in appendix A simplifies the symbolic expressions enough to allow using the full analytical Jacobian and a Newton method. Note that the number of terms and the symbolic complexity of the expressions involved makes the use of symbolic simplification impractical, so a common subexpression elimination strategy is used, where the sub-expressions appearing the most are simplified separately and reused in the code instead of recomputed each time they appear. The EL residuals can also be used in the code, but for them only the numerical inverse of the Leading Order (LO) Jacobian is used as a preconditioner for a Jacobian-free Newton Krylov (JFNK) solve. In what follows, all results presented use the first residuals. We now introduce the following notation: $\alpha=\left\{t_2,\Delta,\{B_l\},P,\{S_k\}\right\}$ denoting the profiles to be solved for on $\hat{r}\in[0;1]$. They are projected onto B-spline FE which in practice is implemented via:

$$\alpha^{(d)}\left(\hat{r}_q\right)=\sum_{i=1}^{m}P_{i,q}^{(d)}\,\alpha^i\,, \tag{2.18}$$

where α^i are the degrees of freedom and $P_{i,q}^{(d)}=\left.\frac{\mathrm{d}^d\Lambda_i}{\mathrm{d}\hat{r}^d}\right|_{\hat{r}=\hat{r}_q}$ denotes the evaluation of the dth derivative of the test (B-spline) function at the quadrature point. It is also understood that for $\alpha=S_k$, the vector of unknowns is augmented by the imposed outer boundary condition at $\hat{r}=1$ (while for the others this is only the case at the axis $\hat{r}=0$). At any radial location, the residuals are given by:

$$R^\alpha=\begin{cases}\left\langle\cos(k\omega)\hat{F}_\psi\right\rangle & \text{if } \alpha\notin\{B_1,\dots B_{N_b},P\}\\ \left\langle\cos(l\omega)(\hat{B}^2-(B_p^2+B_\phi^2))\right\rangle & \text{if } \alpha\in\{B_1,\dots B_{N_b}\}\\ \epsilon^2\hat{r}-\left\langle\hat{J}/\hat{R}^2\right\rangle & \text{if } \alpha=P\end{cases}$$

and project onto the ith FE:

$$R_i^\alpha=\int_0^1 R^\alpha\Lambda_i\mathrm{d}r$$

with $i=1,\dots,m$ denoting each node. The corresponding Jacobian is:

$$J_{i,j}^{\alpha,\gamma}=\int_0^1\left[\frac{\partial R^\alpha}{\partial\gamma}\Lambda_i\Lambda_j+\frac{\partial R^\alpha}{\partial\gamma'}\Lambda_i\Lambda_j'+\frac{\partial R^\alpha}{\partial\gamma''}\Lambda_i\Lambda_j''\right]\mathrm{d}r.$$

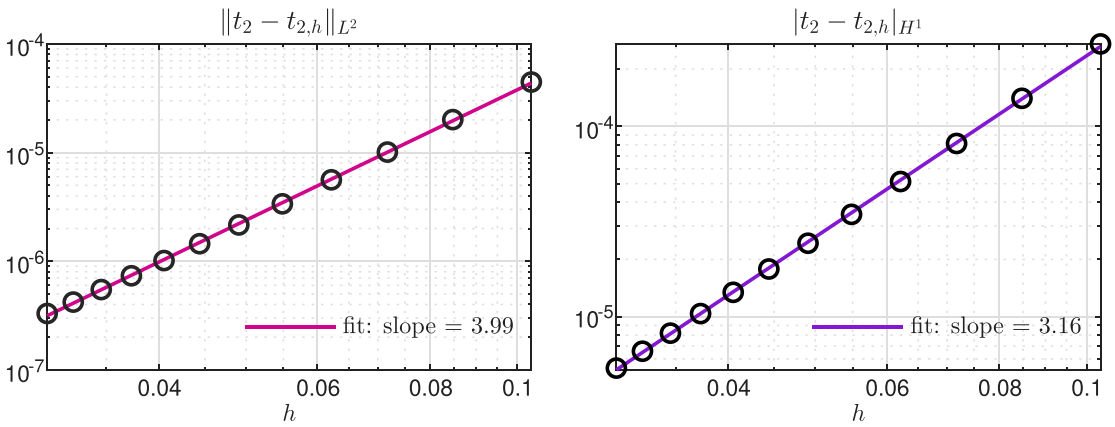


Figure 1. Convergence study for the plasma diamagnetism function t_2 with LO residuals with spline order $p = 3$, number of elements from $m_{\min} = 9$ to $m_{\max} = 31$. h is the geometrical mean of the distance between successive quadrature points.

Discretizing the above integrals via the q quadrature points we get:

$$R_i^\alpha = M_i^q R_q^\alpha, \qquad M_i^q = \Lambda_i(r^q)\, w(r^q), \qquad R_q^\alpha = R^\alpha(r_q)$$

where we keep the two indices (profile, degree of freedom) for clarity, but it is understood that they are flattened before the solver step. Here $w(r^q)$ is the Gaussian weight to approximate the integral above. For the discretized Jacobian, we have:

$$J_{i,j}^{\alpha,\gamma} = M_i^q \mathcal{J}_q^{\alpha,\gamma,(d)} P_{j,q}^{(d)}, \qquad \mathcal{J}_q^{\alpha,\gamma,(d)} = \frac{\partial R^\alpha}{\partial \gamma^{(d)}}$$

The explicit expressions of R^α and $\mathcal{J}^{\alpha,\gamma,(d)}$ are obtained using CAS. The code is written in a modular way, allowing a swap between residual/Jacobian pairs (LO, full, EL), distribution functions (isotropic, rotating, bi-Maxwellian, parallel-rotating), solver (Newton, JFNK). Future work is planned on implementing a spectral discretization instead of FE as the smoothness of the solutions is expected to yield exponential convergence. The default initial guess is: $t_2(\hat{r}) = 0, \hat{\Delta}(\hat{r}) = 0, \hat{P}(\hat{r}) = 0, \hat{B}_\ell(\hat{r}) = 0$ and for the shaping, taken to satisfy the outer imposed BCs $\{\hat{S}_m^{\mathrm{BC}}\}_{m\in[[2;N_S]]}$ via $\hat{S}_m(\hat{r}) = \hat{S}_m^{\mathrm{BC}} \hat{r}^{m-1}$. The code can also be restarted from a given initial guess, which is useful to help convergence in difficult parameter regimes. For B-spline FEs of degree p with maximal continuity C^{p-1}, the FEM approximation satisfies

$$\|u - u_h\|_{L^2} = \mathcal{O}\left(h^{p+1}\right), \qquad |u - u_h|_{H^1} = \mathcal{O}\left(h^p\right), \tag{2.19}$$

provided that the exact solution u is sufficiently smooth, i.e. $u \in H^{p+1}$. In figure 1 a convergence study is presented showing the expected orders 4 and 3 for 3rd order B-splines. The numerical solution of the problem with leading order residuals is compared against the available solution, the leading order analytical solution presented explicitly in section 3.2 and obtained from quadratures. An important remark is that for the full problem we use high order splines $p \geqslant 6$, which is a spectral elements method, because the additional overlap between elements for high order splines helps to regularize the axis residuals which otherwise lead to unconstrained derivatives at the axis. A study like in figure 1 with all profiles is thus even more limited in h values, as the order of convergence is very high and a plateau is reached sooner. The code is free to use and available at: https://github.com/GitGVP/EQUIL/, with the possibility of reproducing all the figures of this article using the dedicated immutable tag.

3. Analytical expansion

In this section the inverse-aspect-ratio expansion is presented in detail. The current treatment differs from previous work allowing in particular the derivation of the higher order corrections seen numerically in section 4 to be required to explain the observed shift and shaping. This treatment differs from prior asymptotic work in three respects. First, the safety-factor profile q and the pressure maps are taken to be exact, independent of ϵ. This choice permits a direct, pointwise comparison between the asymptotic expressions and the full finite-ϵ equilibria solved numerically. Second, results are expressed in terms

of the normalized equation-of-state maps $(\varrho, \Pi_{\|}, \Pi_{\perp})$. Writing results in these variables makes manifest that poloidal pressure variation is functionally constrained by the poloidal dependence of B and R. Third, we emphasize the importance of higher-order corrections which lead to explicit formulae that include anisotropy and rotation and that capture the impact of elongation and triangularity on the shift, as well as the pressure-driven elongation, going one order higher than in the previously published literature.

3.1. Expansion setup

We formally set $\epsilon \ll 1$, and adopt the Tokamak ordering: $\hat{S}_k, \hat{\Delta}, q = \mathcal{O}(1)$. Substituting in equation (2.12) $\beta \to \epsilon^2 \beta$ leads to a regular perturbation theory, as the limit $\epsilon \downarrow 0$ is well defined and boundary conditions can still be satisfied in the limit. This prescription is sometimes misleadingly referred to as the 'low-β ordering' (Freidberg 2014) but we will show in the next sections that it nevertheless allows us to capture high $\beta_p \approx \epsilon^{-1}$[1] effects, albeit at higher order. The ordering used here is consistent with previous literature (Greene *et al* 1971, Connor and Hastie 1985, Graves 2013, Fitzpatrick 2024), in particular, toroidicity effects (Shafranov shift and shaping) appear at an order ϵ lower than the cylindrical part $\epsilon\hat{r}\cos\omega$ in $\hat{R}$ and $\epsilon\hat{r}\sin\omega$ in $\hat{Z}$ which are responsible for the nearest neighbor coupling in the equations. As a result, the shaping does not couple to the shift at LO. This is unlike in e.g. Lao *et al* (1981), Mikhailovskii (1998)and Brunetti *et al* (2020) where the shift prediction takes into account the elongation, but note that in these references, an analytical prediction of the self-consistent shift and shaping is unavailable (i.e. the elongation/triangularity is assumed to be known/prescribed in the shift equation). Since their ordering does not lead to a closed analytic hierarchy for the geometry, it is not well suited to the present goal of deriving explicit higher-order corrections. Moreover, while shaping could formally be promoted to lower order (alongside the $\epsilon\hat{r}\cos\omega$ term), the physical effects on instabilities are unchanged at the relevant order, as can be seen by comparing the shaping contributions in Eriksson and Wahlberg (2002) with those in Brunetti *et al* (2020); the ordering adopted here instead enables a formal order-by-order Fourier decomposition in which the geometric coefficients separate and their radial profiles are determined self-consistently. A further remark is that from our assumptions above, the fact that $\hat{P}, t_2 = \mathcal{O}(1)$ is a consequence of their respective LO equation. Physically, lowering ϵ should be interpreted as straightening the device, not as a near axis expansion which corresponds to setting $\hat{r} \ll 1$. The latter allows to obtain axis regularity boundary conditions: the assumption that $\hat{r} = 0$ corresponds to a magnetic axis (i.e. a parabolic point of ψ) means that locally, flux surfaces are concentric ellipses, giving in our coordinates:

$$\begin{aligned}\hat{R}(\hat{r},\omega) &= 1 + \epsilon\hat{r}\left(1 + \epsilon\frac{\mathrm{d}\hat{S}_2}{\mathrm{d}\hat{r}}\bigg|_{\hat{r}=0}\right)\cos\omega + \mathcal{O}\left(\hat{r}^2\right)\\ \hat{Z}(\hat{r},\omega) &= \epsilon\hat{r}\left(1 - \epsilon\frac{\mathrm{d}\hat{S}_2}{\mathrm{d}\hat{r}}\bigg|_{\hat{r}=0}\right)\sin\omega + \mathcal{O}\left(\hat{r}^2\right)\end{aligned} \tag{3.1}$$

which, on top of the mentioned axis BC in section 2 leads to $\Delta'(0) = S'_{k\geqslant 3}(0) = 0$ for physically acceptable forcing (i.e. vanishing axis pressure gradients and magnetic shear). We construct truncated solutions to order N, assuming that all unknowns admit regular expansions in ϵ:

$$\begin{aligned} t_2(\hat{r}) &= \sum_{k\geqslant 0}^{N} t_{2,k}(\hat{r})\,\epsilon^k, \quad \hat{\Delta}(\hat{r}) = \sum_{k\geqslant 0}^{N} \hat{\Delta}_k(\hat{r})\,\epsilon^k,\\ \hat{S}_m(\hat{r}) &= \sum_{k\geqslant 0}^{N} \hat{S}_{m,k}(\hat{r})\,\epsilon^k, \quad \hat{P}(\hat{r}) = \sum_{k\geqslant 0}^{N} \hat{P}_k(\hat{r})\,\epsilon^k. \end{aligned}$$

Collecting powers of ϵ yields, at each order k, a linear second-order ODE of the form $\mathcal{L}y_k = f_k$, with $\mathcal{L}$ a linear differential operator that is independent of the order k, while f_k is an inhomogeneous term which depends on previous order solutions $(y_{k-1}, y_{k-2}, \dots)$. The general solution is

$$y_k(\hat{r}) = c_{1,k}y_1(\hat{r}) + c_{2,k}y_2(\hat{r}) + y_{\mathrm{part},k}(\hat{r})$$

with $y_{1,2} \in \ker\mathcal{L}$ (i.e. such that $\mathcal{L}y_{1,2} = 0$). Boundary conditions determine the coefficients $c_{i,k}$. For $(t_2, \hat{\Delta}, \hat{P})$ the physical BCs are homogeneous and enforced identically at every order; the homogeneous

[1] In this article $\sim$ is used to define an asymptotic relation, strictly valid after passing to the limit, while $\approx$ refers to a pointwise (or uniform) order of magnitude equality.

coefficients are therefore fixed accordingly. For the shaping modes $\hat{S}_m$ two prescriptions were tested. The first sets all higher-order homogeneous coefficients to zero and retains only the particular solutions, adapting the $k=0$ regular solution coefficient to the higher order's contributions at the edge to match the prescribed outer BC. The second keeps the free homogeneous coefficients at higher orders and uses them to enforce homogeneous BCs at orders $k \geqslant 1$. The latter method produces noticeably better agreement in our numerical tests and is adopted in what follows. Expanding $\hat{F}_\psi$ order by order in ϵ yields the relevant differential operators determining the unknowns. For t_2 this is:

$$\mathcal{L}_{\text{dia}} = \hat{r}q^2 \frac{\mathrm{d}}{\mathrm{d}\hat{r}} \Rightarrow \mathcal{L}_{\text{dia}}^{-1}[F] = \int_0^{\hat{r}} \mathrm{d}s \frac{F(s)}{sq(s)^2}.$$

Having imposed $t_2(0)=0$ for the inverse. Relevant physical forcing are such that $F \sim r^2$ near the axis which is sufficient to avoid singularities. It is seen that increasing the q profile at a constant aspect ratio means increasing the ratio B_ϕ/B_p and more forcing is required to reach the same amount of diamagnetism. For the shift ($\hat{\Delta}$) equation, we instead have:

$$\mathcal{L}_\Delta = \frac{\mathrm{d}}{\mathrm{d}\hat{r}}\left(\frac{\hat{r}^3}{q^2}\frac{\mathrm{d}}{\mathrm{d}\hat{r}}\right) \Rightarrow \mathcal{L}_\Delta^{-1}[F] = \int_0^r \mathrm{d}t \frac{q(t)^2}{t^3}\int_0^t \mathrm{d}s\,(F(s))$$

where in the inverse we have enforced $\hat{\Delta}(0)=0$ and axis regularity. Here, on the contrary the forcing gets enhanced by q^2, which can be intuitively understood as a smaller poloidal field (higher q) being easier to shape. It will be seen in the following section that the forcing that arises from geometrical coupling will also be proportional to q^{-2} and therefore will be weakly affected by the value of the safety factor, unlike the pressure drive. For the general shaping ($\hat{S}_m$), an explicit inverse for arbitrary q profile is not available:

$$\mathcal{L}_m = \frac{\mathrm{d}}{\mathrm{d}\hat{r}}\left(\frac{\hat{r}^3}{q^2}\frac{\mathrm{d}}{\mathrm{d}\hat{r}}\right) - \hat{r}\frac{m^2-1}{q^2}.$$

Here it is useful to comment on diverted equilibria, which exhibit a logarithmically divergent safety factor $q \sim -\log(1-\hat{r})$. The results of the current analysis can be shown to be valid also for these equilibria, provided the analysis is carried up until some threshold, e.g. the engineering r_{95}, as the remainder contribution can be shown to be vanishingly small with distance δ from the plasma-vacuum interface. For the shaping, since it is smooth between r_{95} and $r=a$, the boundary conditions can be safely imposed at r_{95} instead, treating the plasma as a limited one. In this work, we treat only plasmas with a maximum $q \leqslant 10$ for this reason. For the pressure-related forcings, following section 2.2, they can all be expressed in terms of derivatives of the map $\Pi_\parallel$ as e.g.

$$\frac{\partial \bar{\beta}_\parallel}{\partial \hat{r}} = \frac{\mathrm{d}}{\mathrm{d}\hat{r}}\Pi_\parallel\left(\hat{r}, \hat{B}(\hat{r},\omega), \hat{R}(\hat{r},\omega)\right) = \left(\frac{\partial \Pi_\parallel}{\partial \hat{r}}\right)_{\hat{R},\hat{B}}\Bigg|_{\hat{R}=1,\hat{B}=1}[1+\mathcal{O}(\epsilon)]$$

and the expansion in ϵ is related to that of $(\hat{R},\hat{B})$ only. Note in particular that this formulation is significantly different to what is done in Greene *et al* (1971), Madden and Hastie (1994), Fitzpatrick (2024), where the pressure profile is also assumed to have a series representation $p(r) = \epsilon^2 p_2(r) + \epsilon^3 p_3(r) + \ldots$, with only $p_2(r)$ assumed to be the known forcing. Their prescription leads to an underdetermined system at higher order and is also more difficult to validate against finite-ϵ simulations. At leading order, the first derivatives of $\Pi_\parallel$ can be substituted using equation (2.15) making the total dynamical pressure $(p_\parallel + p_\perp + \rho R^2\Omega^2)$ appear, while at higher order 2nd derivatives appear which do not have a simple intuitive meaning. In the next section, we explicit the leading order forcings $F_{\text{dia}}, F_\Delta, F_m$, show the solutions when available explicitly, followed in the next section by the novel higher order effects.

3.2. Leading order

The leading order flux averaged force balance leads to:

$$t_2(\hat{r}) = \int_0^{\hat{r}} \mathrm{d}s \frac{s}{q(s)^2}\left(s\frac{q'(s)}{q(s)} - 2\right) - \left(\Pi_\parallel(\hat{r},\hat{B}=1,\hat{R}=1) - \Pi_\parallel(0,\hat{B}=1,\hat{R}=1)\right) \tag{3.2}$$

which is related to the plasma diamagnetism via (restoring dimensions):

$$RB_\phi(r,\omega) = R_0 B_0\left(1 - \epsilon^2\left[\frac{r^2}{2q^2} + \int_0^r \mathrm{d}s \frac{s}{q(s)^2} - \frac{\mu_0}{B_0^2}(P_\perp - P_{\perp,0})\right]\right) + \mathcal{O}(\epsilon)^4 \tag{3.3}$$

with $P_{\perp,0}$ the perpendicular pressure at the axis and we have integrated by parts to make manifest that the two terms in the square brackets involving the q profile are strictly positive. The poloidal dependence is seen to come only at higher order. Equation (3.3) is extremely important for equilibrium reconstruction, as it shows that measurements related to the toroidal field such as the plasma toroidal diamagnetic flux are insensitive to the parallel component of the pressure, and may therefore allow isotropic and anisotropic discharges to be discerned. Next, the $m = 1$ harmonic corresponding at this order to the force balance in the ∇R direction, gives the shift of the flux surfaces:

$$\mathcal{L}_\Delta[\Delta] = \frac{\hat{r}^3}{q^2} - 2\hat{r}^2 \frac{\partial}{\partial \hat{r}} \left(\frac{\Pi_\parallel + \Pi_\perp}{2} + \frac{1}{2} \varrho \hat{R} \Omega^2 \right).$$

Restoring dimensions, it is seen that a simple generalization of the isotropic formula is valid:

$$\frac{\mathrm{d}\Delta}{\mathrm{d}r} = \frac{r}{R_0} \left(\bar{\beta}_p(r) + \frac{\ell_i(r)}{2} \right)$$

with the definitions:

$$\bar{\beta}_p(r) = -\frac{q^2}{r^4} \frac{\mu_0 R_0^2}{B_0^2} \int_0^r \mathrm{d}s \left[s^2 \frac{\partial}{\partial s} \left(P_\parallel + P_\perp + \rho R^2 \Omega^2 \right)_{R=R_0, B=B_0} \right], \quad \ell_i(r) = 2\frac{q^2}{r^4} \int_0^r \mathrm{d}s \frac{s^3}{q^2}.$$

For the specific isotropic rotating case, the pressure drive becomes $-\hat{r}^2 \left[(1 + 2\mathcal{M}^2) \beta_0 \right]'$, with the factor 2 coming from one contribution related to the centrifugal term $\rho(\boldsymbol{u} \cdot \nabla)\boldsymbol{u}$ and the other to the pressure gradient ∇p. We define $\beta_{p,\mathrm{int}}$ as the integrand in the definition of $\bar{\beta}_p$ as this combination of pressures will again appear in the next section. This analysis is relevant for equilibrium reconstruction, as the poloidal magnetic field is given by:

$$B_p = \epsilon \frac{r B_0}{q(r)} \left(1 - \epsilon (r - \Delta') \cos\omega + \epsilon \cos\omega \sum_{k \geqslant 2} S_k'(r) \cos[(k-1)\omega] - \epsilon \sin\omega \sum_{k \geqslant 2} S_k'(r) \sin[(k-1)\omega] \right)$$

so that flux loops and magnetic probes measuring B_p outside the plasma can infer the total enclosed Shafranov parameter $\bar{\beta}_p + \ell_i/2$.

Here we stress what we mean by 'Tokamak ordering', in the expression for B_p both factors ϵ and r can be seen, the former means that in straightening the Tokamak ($\epsilon \to 0$) the considered limit is that of the $\theta-$pinch and not of the general screw pinch (because we want to keep q fixed in this variation for stability applications), while the latter is consistent with the vanishing of the poloidal field at the axis ($r \to 0$). For the shaping, the leading order forcing vanishes, leading to

$$\mathcal{L}_m \left[\hat{S}_m \right] = 0$$

meaning that the only drive at leading order is the coil-imposed outermost surface shaping, which is significant for modern Tokamaks. A useful special case is obtained for constant$-q$, leading to $\hat{S}_m = \hat{S}_m^{\mathrm{BC}} \hat{r}^{m-1}$ with $\hat{S}_m^{\mathrm{BC}}$ the imposed boundary harmonic. This simple result is used to gain intuition on the results of the next section, and is shown in the numerical simulations to be a reasonably good approximation even when q is not constant. The LO prediction for $\hat{P}$ has been given in Graves (2013) and since this profile serves as gauge fixing, all physical predictions can be expressed without explicitly invoking it.

3.3. Higher order effects

In this section we focus on the two most important effects that come at the NLO, namely the shaping-driven shift and the pressure driven elongation. In what follows, we assume that the boundary shaping is such that $\hat{S}_2, \hat{S}_3 \gg \hat{S}_{m \geq 4}$, that is we consider experimentally relevant elongated D-shaped (outwards or inwards) cross sections, while higher harmonics would contribute a minor correction. For the shift, we split the contributions into $F_\Delta = F_{\Delta,\mathrm{geom}}/q^2 + F_{\Delta,\beta}$, the first coming from purely geometrical coupling:

$$F_{\Delta,\mathrm{geom}} = \hat{r}\hat{S}_{2,0}' \left(10\hat{S}_{3,0} - \hat{r} \left(\hat{r} + (1 - 3s)\hat{S}_{3,0}' + 3(s-1)\hat{\Delta}_0' \right) \right) + \hat{S}_{2,0} \left(\hat{r} \left(5\hat{S}_{3,0}' - 3\hat{\Delta}_0' \right) - 2\hat{S}_{3,0}(s-7) \right) \tag{3.4}$$

where we have neglected terms like $-\hat{r}\hat{S}_{4,0}'(14\hat{S}_{3,0} + \hat{r}\hat{S}_{3,0}')$ and other coupling $\hat{S}_{m,0}\hat{S}_{m\pm1,0}$ from the assumption of small squareness and higher harmonics above. The pressure driven contribution is:

$$F_{\Delta,\beta} = \frac{3}{2} \frac{1}{\hat{r}} \left(\hat{S}_{2,0} + \hat{r}\hat{S}_{2,0}' \right) \beta_{p,\mathrm{int}}.$$

Both contributions vanish for non-elongated plasmas $\hat{S}_{2,0} = \hat{S}'_{2,0} = 0$, while for conventionally elongated cross sections $\hat{S}_{2,0}, \hat{S}'_{2,0} < 0$ the shift is usually reduced (monotonic pressures $\partial_{\hat{r}}\bar{p} < 0$, positive triangularity $\hat{S}_{3,0} > 0$) as found in Lao *et al* (1981). Using the zero-shear replacement for the shaping ($\hat{S}_{2,0} = \hat{S}_2^{\mathrm{BC}}\hat{r}, \hat{S}_{3,0} = \hat{S}_3^{\mathrm{BC}}\hat{r}^2$) we find that the contribution from triangularity, i.e. terms containing $\hat{S}_{3,0}$ or $\hat{S}'_{3,0}$ in equation (3.4) lead to $-32\hat{r}^3\hat{S}_2^{\mathrm{BC}}\hat{S}_3^{\mathrm{BC}}$, having also neglected the shear term here, which is in general smaller. The dimensionless numerical prefactor 32 makes the NLO shift very sensitive to the triangularity. The main conclusions for the shift are that the elongation is the main driver of this term, if the cross section is elongated then it is the same combination of pressures in $\beta_{p,\mathrm{int}}$ that contribute, and finally that the coupling with triangularity is strong. For the elongation, we split again the forcing into $F_\kappa = F_{\kappa,\mathrm{geom}}/q^2 + F_{\kappa,\beta}$, with expressions:

$$F_{\kappa,\mathrm{geom}} = \hat{\Delta}'_0\left(1 + (2-3s)\,\hat{S}'_{3,0} - 8\frac{\hat{S}_{3,0}}{r}\right) + \frac{1}{2}\left(\hat{r} - 2\hat{S}'_{3,0}\right) + \frac{3}{2\hat{r}}(s-2)\,\hat{\Delta}_0'^2$$

and

$$\begin{aligned} F_{\kappa,\beta} = {} & \frac{q^2}{\hat{r}^3}\left(6\left(\hat{\Delta}'_0 - \hat{S}'_{3,0}\right) - \hat{r} - 8\frac{\hat{S}_{3,0}}{\hat{r}}\right)\beta_{p,\mathrm{int}} \\ & + \frac{q^2}{4}\frac{\partial}{\partial\hat{r}}\left[3\varrho\hat{R}\Omega^2 + \left(\Pi_\perp - \Pi_\parallel\right) + \frac{\partial^2\Pi_\parallel}{\partial\hat{R}^2} - 2\frac{\partial^2\Pi_\parallel}{\partial\hat{R}\partial\hat{B}} + \frac{\partial^2\Pi_\parallel}{\partial\hat{B}^2}\right] \end{aligned} \tag{3.5}$$

where $F_{\kappa,\mathrm{geom}}$ is the same for any plasma model (isotropic, etc), and the first line of equation (3.5) is the pressure drive that depends on the same combination as the shift, while the second line is different and only present in the case of anisotropy and or rotation. It is interesting to note that the cross derivative term $\partial_{R,B}P_\parallel$ is an effect that is present only when both rotation and anisotropy are taken into account. For the special case of constant$-q$ and parabolic pressure profiles, all the operators are analytically invertible and one can obtain from CAS software solutions up to arbitrary ordering ϵ. We show this in appendix B to illustrate some properties of the expanded solutions explicitly.

4. Numerical results

In this section, we present numerical results illustrating the geometry and plasma diamagnetism in conventional aspect ratio equilibria, for isotropic, strongly perpendicularly anisotropic, and rotating parallel anisotropic plasmas. We do not study the perpendicular anisotropic rotating case as it is less experimentally relevant, and would require a more accurate treatment of quasineutrality. The results are illustrated with aspect ratio scans, validating the LO predictions from section 3.2 and the NLO ones from section 3.3. To compare the numerical results with the analytical ones, we define the following errors: the LO error is:

$$\|\hat{\Delta}_{\mathrm{num}} - \hat{\Delta}_0\|_{L^2}^2 := \int_0^1 \left(\hat{\Delta}_{\mathrm{num}} - \hat{\Delta}_0\right)^2 \mathrm{d}\hat{r} \tag{4.1}$$

and similar definitions hold for the other profiles $(t_2, S_m, \dots)$. The NLO error is defined by:

$$\|\hat{\Delta}_{\mathrm{num}} - \hat{\Delta}_0 - \epsilon\hat{\Delta}_1\|_{L^2}^2 := \int_0^1 \left(\hat{\Delta}_{\mathrm{num}} - \hat{\Delta}_0 - \epsilon\hat{\Delta}_1\right)^2 \mathrm{d}\hat{r} \tag{4.2}$$

the expected order of convergence in ϵ are respectively 1 for the LO error and 2 for the NLO one, as verified in the following sections. Note that we do not include the Jacobian in the radial measure i.e. we use $\mathrm{d}\hat{r}$ instead of $\hat{J}\mathrm{d}\hat{r}$, as this would involve non-trivially the unknowns and change the aspect ratio scaling. We first present briefly a comparison of the code, the LO prediction and Solov'ev full solutions for isotropic rotating plasmas at high aspect ratio $A = 10$, acting as a benchmark for the code and showing the magnitude of deviations compared to the LO prediction even at such high aspect ratios. Next, we present a TCV-like shaped isotropic case, to show the magnitude of the deviation from analytical predictions, followed by cases of fully parallel anisotropic rotating plasmas, showing that the toroidal diamagnetism is similar to pressureless equilibria, while the shafranov shift is strongly affected by the pressure and the rotation. Finally, we show very strongly perpendicularly anisotropic equilibria, for which it is shown that the pressure-driven shaping remains small compared to the LO prediction in shaped plasmas.

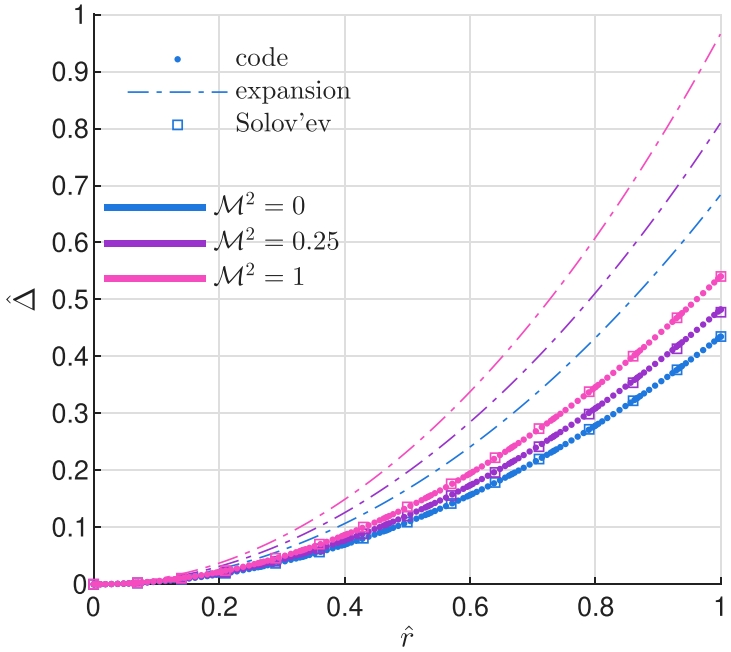


Figure 2. Normalized shift for elongated equilibria comparing the code output (dots), the Solov'ev output (dashes), and the LO prediction (dash-dotted), for various rotation levels.

4.1. Comparison with rotating Solov'ev equilibria

We confine to appendix E the details of the construction of the analytical rotating Solov'ev solution for prescribed boundary shaping, as well as the method used to retrieve the shaping coefficients from equation (2.8). Given that the structure of the Solov'ev solutions limits the possibility of performing aspect ratio scans, we fix $A \approx 8$ and assess the validity of the code by varying the rotation strength, focusing here on the shift to provide a concise assessment. We construct an elongated equilibrium corresponding to $\hat{S}_2^{\text{BC}} = -1.7$ and compare in figure 2 the normalized shift $\hat{\Delta} = \Delta/(\epsilon a)$ predicted by the code with those from the Solov'ev solution and the LO expansion. Both the safety factor and the pressure profiles are quadratic in $\hat{r}$, leading to $\beta_p \approx 0.9$ and $w_\phi \approx 0, 0.2, 0.7$ for $\mathcal{M}^2 = 0, 0.25, 1$ respectively. The code shows excellent agreement with the Solov'ev profiles, whereas the LO prediction exhibits a visible deviation despite the high aspect ratio, as it does not account for the shift reduction related to the elongation, analyzed in the next section.

4.2. Isotropic plasmas

Here we study an isotropic static plasma ($\Omega = 0, p_\parallel = p_\perp$) by doing an aspect ratio scan, from $\epsilon = 10^{-3}$ to $\epsilon = 0.4$ and showing the L^2 error for the leading order and NLO shaping (Δ, S_2). The diamagnetism profile t_2 will be analyzed in more detail in the next sections. We use a parabolic pressure profile $\beta(\hat{r}) = \beta_{t0}(1 - \hat{r}^2)$ as well as a parabolic q profile $q(\hat{r}) = q_0(1 + s_0\hat{r}^2/2)$. The simulation parameters are $\beta_{t,0} = 0.8, q_0 = 1, s_0 = 4, \hat{S}_2^{\text{BC}} = -0.8, \hat{S}_3^{\text{BC}} = 0.2$ and are held constant during the aspect ratio scan. These are chosen such that at $\epsilon = 0.4$, we have $\beta_p = 1.7, \ell_i = 0.8, \kappa = 1.9, \delta = 0.4$, with $q_{95} \approx 3$, according to the definitions in appendix D which are realistic TCV plasma values. In particular, these choices are in the high range of plasma betas and shaping, which are far from an almost circular, low β ohmic discharge. Figure 3 presents the convergence plot for the L^2 error (equations (4.1) and (4.2)) for the Shafranov shift on the left and for the elongation on the right, for $\epsilon \in [10^{-3}; 0.4]$. The expected first and second orders of convergence are verified. For the shift, the NLO correction is seen to significantly improve the LO prediction, dropping the error by a factor 10 for conventional aspect ratio $\epsilon \approx 0.4$. The corresponding shift profiles are shown in figure 4, where the LO (left) and NLO (right) analytical prediction is shown as a black dashed line. The colored lines correspond to the numerical solution $\hat{\Delta}_{\text{num}}$ on the left and the numerical NLO correction, defined via:

$$\hat{\Delta}_{1,\text{num}} := \frac{\hat{\Delta}_{\text{num}} - \hat{\Delta}_0}{\epsilon} \tag{4.3}$$

which is introduced to compare against the analytical prediction $\hat{\Delta}_1$. The colors correspond to the aspect ratios of figure 3. The pink dashed line on the left figure shows the LO and NLO correction for the

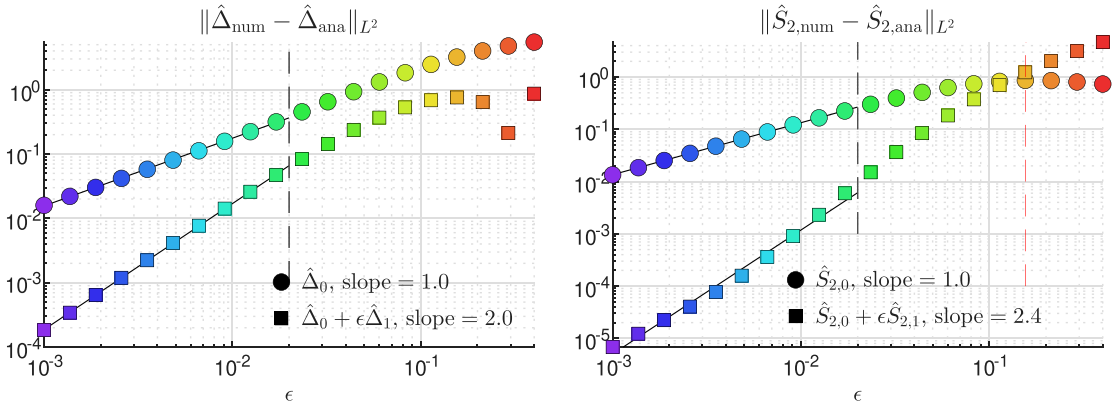


Figure 3. Normalized Shafranov shift (left) and elongation (right) convergence plots in aspect ratio for both leading order (circles) and next to leading order (squares) prediction for the isotropic equilibrium. Linear fits are done up to the black dashed vertical line at $\epsilon_1 = 0.02$. The red dashed vertical line at $\epsilon_2 = 0.16$ shows where the LO prediction has a lower error than the NLO prediction for the elongation.

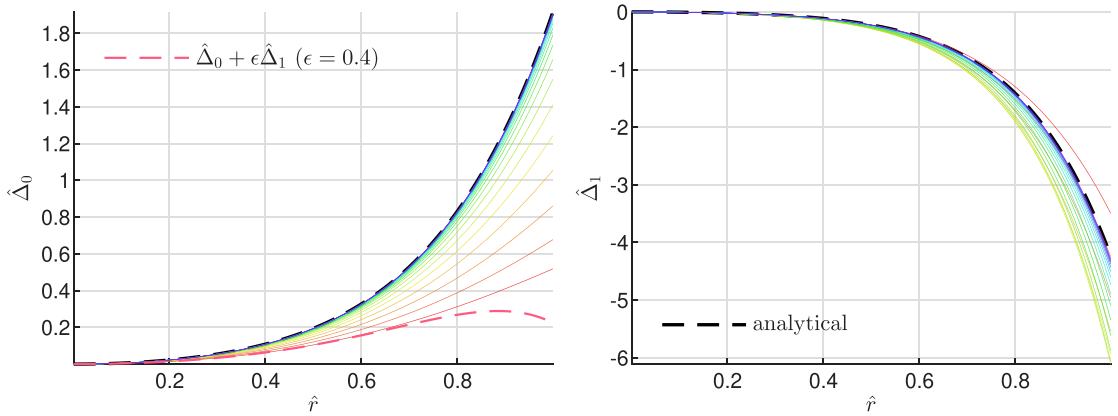


Figure 4. Normalized Shafranov shift. Colored lines are the numerical solutions, with aspect ratio of figure 3. The analytical predictions are in dashed black, for the LO (left) and the NLO correction (right). The full NLO prediction is shown in pink on the left plot for the highest $\epsilon = 0.4$.

highest $\epsilon = 0.4$, to be compared with the red line, which significantly deviates from the LO prediction. The finite-ϵ shift reduction observed numerically is well explained by the NLO prediction. Figures 3 and 4 thus show that the NLO correction is a significant improvement on the LO prediction for conventional aspect ratio tokamaks with outer elongation and triangularity, as the error to the full solution goes from $\|\hat{\Delta} - \hat{\Delta}_0\|_{L^2} \approx 5$ to $\|\hat{\Delta} - \hat{\Delta}_0 - \epsilon\hat{\Delta}_1\|_{L^2} \approx 0.8$ for $\epsilon = 0.4$. Conversely, the left plot in figures 3 and 5 show the same analysis for the elongation. There the conclusions are significantly different: even though the predicted order of convergence is found, it is observed that $\|\hat{S}_{\text{num}} - (\hat{S}_{2,0} + \epsilon\hat{S}_{2,1})\|_{L^2} > \|\hat{S}_{\text{num}} - \hat{S}_{2,0}\|_{L^2}$ for $\epsilon > 0.15$, meaning that for experimentally relevant aspect ratios, the LO prediction for the shaping is a more accurate approximation than the NLO one. These results illustrate that with the current formulation of the expansion, and of the underlying equations, scans in ϵ to assess the validity of the error bounds of the expansion are simplified: the leading order solution does not depend on ϵ due to the rescalings of section 2.1.

4.3. Strong parallel anisotropy with near sonic flows

In this section we analyze with the full code a conventional aspect ratio $\epsilon = 0.35$ elongated negative triangularity $(\delta = -0.41, \kappa = 1.74)$ plasma, comparing various cases with or without rotation and with or without strong parallel anisotropy. Figure 6 shows the flux surfaces as well as the parallel normalized pressure contours for the case without perpendicular pressure and no rotation on the left, with sonic rotation in the middle, and the normalized pressure contour for the isotropic rotating case with sonic rotation on the left. Note that $\mathcal{M}^2 = 1$ is higher than the rotation expected to be seen in TCV and conventional aspect ratio tokamaks. For the parallel anisotropic case $(p_\perp = 0)$, the pressure contours are

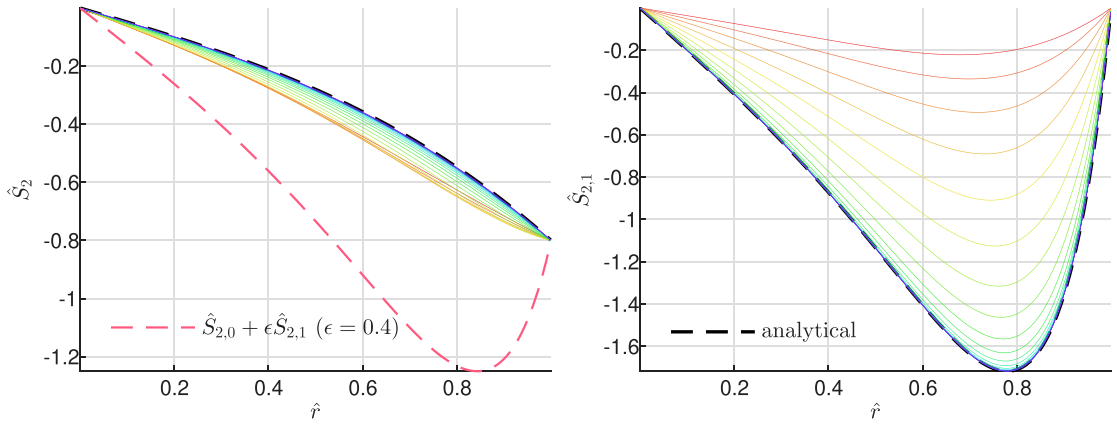


Figure 5. Normalized elongation. Colored lines are the numerical solutions, with aspect ratio of figure 3. The analytical predictions are in dashed black, for the LO (left) and the NLO correction (right). The full NLO prediction is shown in dashed pink on the left plot for the highest $\epsilon = 0.4$.

slightly shifted towards the HFS, while the opposite is true for the rotating isotropic case, and the parallel rotating case has a combination of both effects. The figure also displays the TCV limiter contour to show that the boundary conditions and aspect ratio used ($\epsilon = 0.35, \hat{S}_2^{\text{BC}} = -0.8, \hat{S}_3^{\text{BC}} = -0.3$) correspond to realistic parameters. Figure 7 instead shows the profile of diamagnetism, shift, and plasma driven elongation from the full code. From the diamagnetism plot, we see that the pressureless case and the fully parallel cases (rotating or not) are very close to each other, which is coherent with the notion that perpendicular pressure is responsible for the plasma diamagnetism. On the other hand, for the shift and elongation which characterize the poloidal field, the pressureless case is different to all the other cases, and the parallel anisotropic and isotropic rotating cases are overlapping. This means that in this case the poloidal field is modified significantly by the rotation and its contribution to the dynamical pressure $\rho R^2\Omega^2$. The effect of the plasma on the poloidal field is well described by the plasma's Shafranov parameter: $\beta_{p,\parallel} + \beta_{p,\perp} + w_\phi + \ell_i/2$, which is $\approx$3 for the similarly shifted rotating isotropic and rotating parallel anisotropic, while it is $\approx$2 for the static parallel anisotropic case, and $\approx$0.7 for the pressureless case. It is remarkable that both the isotropic ($\mathcal{M}^2 = 1$) and parallel rotating cases ($\beta_\perp = 0, \mathcal{M}^2 = 1$) have nearly identical flux contours, as expected from their similar Shafranov parameter, but completely opposite diamagnetism, which means that isotropic static equilibrium reconstruction codes which use the total plasma toroidal diamagnetic flux Φ_p and magnetic probes and flux loops would receive opposite information from the two diagnostics. This will be investigated more in detail in a following publication.

4.4. Strong perpendicular anisotropic discharges

In this section we study a case representative of ICRH heating and that should exhibit perpendicular anisotropy-driven shaping as predicted in Madden and Hastie (1994). To do so, we analyze a conventional aspect ratio ($\epsilon = 0.37$) circular equilibrium ($\delta = 0, \kappa = 1$) which means that $\hat{S}_{2,0} = 0$ as a result of the homogeneous BCs, and $\hat{\Delta}_1 = 0$ as shown in section 3.3. The distribution function used is the modified bi-Maxwellian from equation (2.16) and we model a low field side (LFS) resonance by choosing $\hat{B}_c = 0.98$. The $q(\hat{r})$ profile and $\beta(\hat{r})$ are obtained from fitting those of an isotropic test case of the MEQ suite (Carpanese 2021), via polynomials of the form $q(\hat{r}) = 1 + \sum_{k=1}^{10} q_k \hat{r}^{2k}$ and $\beta(\hat{r}) = \sum_{k=0}^{10} \beta_k \hat{r}^{2k}$. The obtained profiles yield $q(1) \approx 5.3, \beta(0) = 0.19$ corresponding to $\beta_p = 2, \ell_i = 1.14$ according to the definitions given in section D. We set $T_\perp/T_\parallel = 3$ corresponding to $\beta_{p,\perp}/\beta_{p,\parallel} \approx 2.9$, so that we are in the regime $\epsilon T_\perp/T_\parallel \sim 1$ described in Madden and Hastie (1994). Figure 8 shows the contours of the magnetic field strength and the normalized perpendicular pressure, the parallel one being much smaller. These are obtained from simulations with $N_S = 10, N_B = 10$ the number of shaping harmonics and field harmonics respectively. On the field strength plot, we can see the bending of the vertical contours inwards where the pressure is highest, which is the typical cylindrical Z-pinch pressure balance between pressure and diamagnetism. The contour $B = B_c$ is shown in green on both plots. On the perpendicular pressure plot, the strong poloidal localization of the pressure towards the LFS is manifest. Figures 9 and 10 show a convergence study from $\epsilon = 0.37$ to $\epsilon = 10^{-3}$ similar to that done for the isotropic case

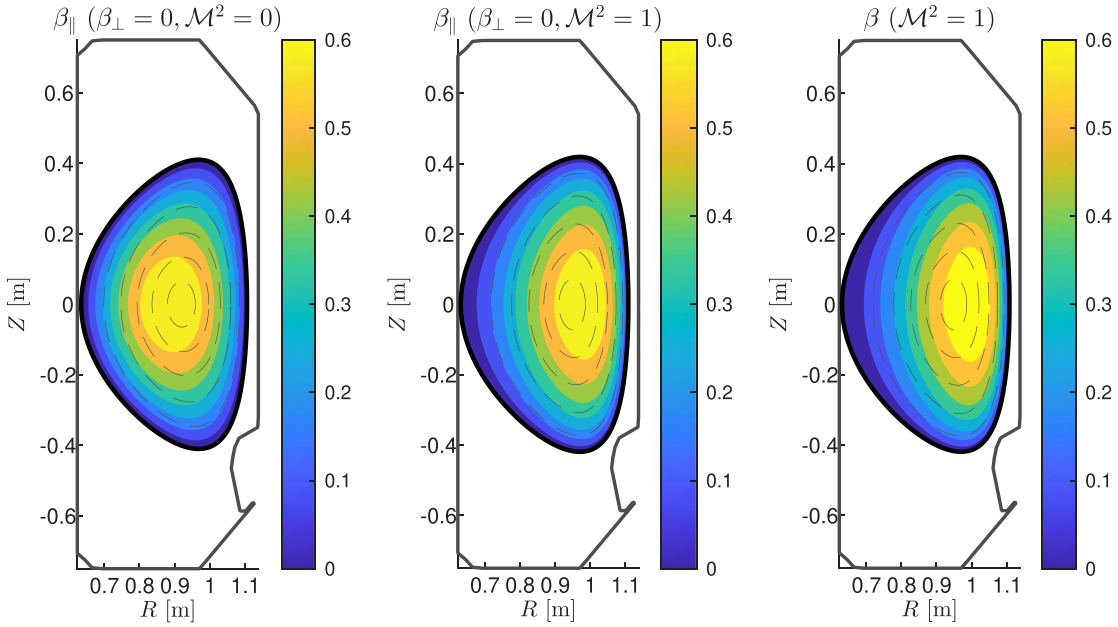


Figure 6. Flux surface contours (dashed black) and normalized pressures contours (colors) for the parallel static case (left), parallel rotating (middle) and isotropic ($\mathbb{P} = p\mathbb{I}$) rotating case (right), obtained from the full code, in the TCV vacuum vessel.

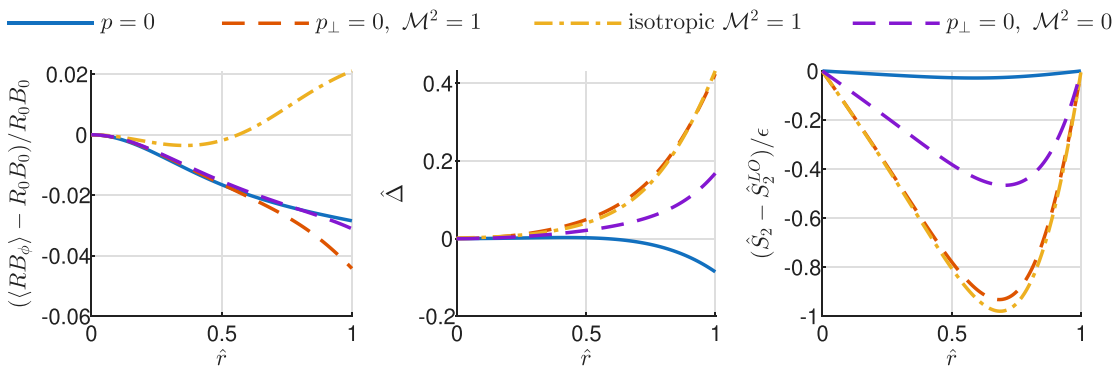


Figure 7. Plasma diamagnetism, shift and plasma driven elongation, for a negative triangularity TCV-like shaping. Pressureless case (blue), fully parallel with sonic rotation (orange), isotropic with sonic rotation (yellow) and fully parallel static case (purple).

in section 4.2. In figure 9 the orders now are 2 and 3 since $\hat{\Delta}_1 = 0$ as well as $\hat{S}_{2,2} = 0$ for non-shaped boundaries. This is verified also analytically in appendix B where it is seen that $\hat{S}_{2,2} \propto \hat{S}_2^{\text{BC}}$. In spite of the high order of convergence of the error, the numerical solution at $\epsilon = 0.37$ significantly deviates from the analytical predictions. The flux surfaces predicted by the expansion would in fact intersect due to the highly overestimated shift shear $\hat{\Delta}'$ and elongation shear $\hat{S}_2'$. We note that these observations are very similar to high β_p isotropic cases, as presented in section 4.2. For this case also we have that $\|\hat{S}_{\text{num}} - (\hat{S}_{2,0} + \epsilon\hat{S}_{2,1})\|_{L^2} > \|\hat{S}_{\text{num}} - \hat{S}_{2,0}\|_{L^2}$ for $\epsilon > 0.15$, so that the NLO prediction for the elongation should not be used for relevant aspect ratio.

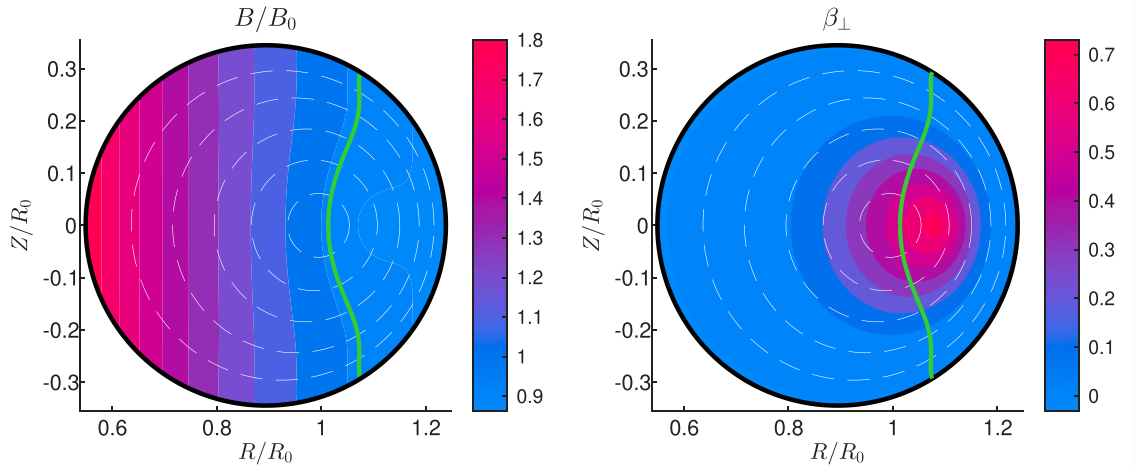


Figure 8. Normalized magnetic field strength and perpendicular pressure contours for a circular equilibrium ($\delta = 0, \kappa = 1$) with resonance at the LFS $B_\epsilon/B_0 = 0.98$ (in green) and strong perpendicular anisotropy ($\epsilon = 0.37, T_\perp/T_\parallel = 3, \epsilon T_\perp/T_\parallel = 1.1$).

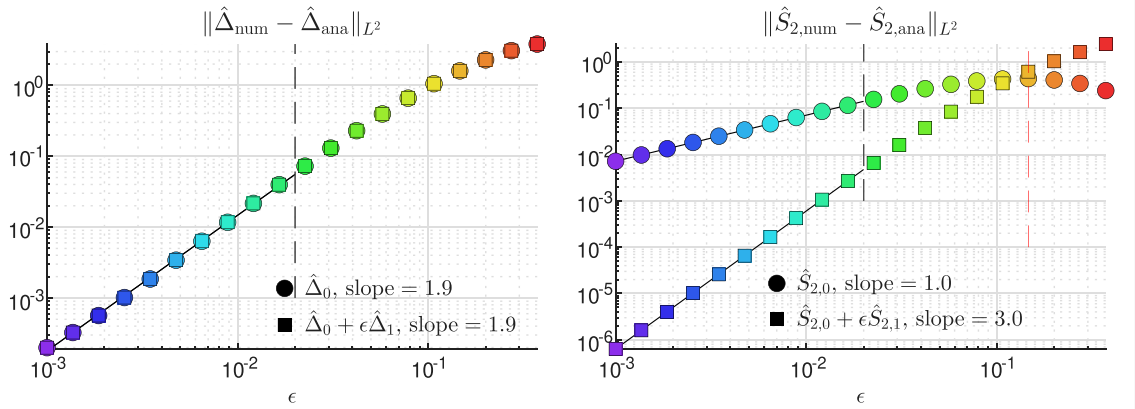


Figure 9. Normalized Shafranov shift (left) and elongation (right) convergence plots in aspect ratio for both leading order (circles) and next to leading order (squares) prediction for the anisotropic circular equilibrium. Linear fits are done up to the black dashed vertical line at $\epsilon_1 = 0.02$. The red dashed vertical line at $\epsilon_2 = 0.16$ shows where the LO prediction has a lower error than the NLO prediction for the elongation.

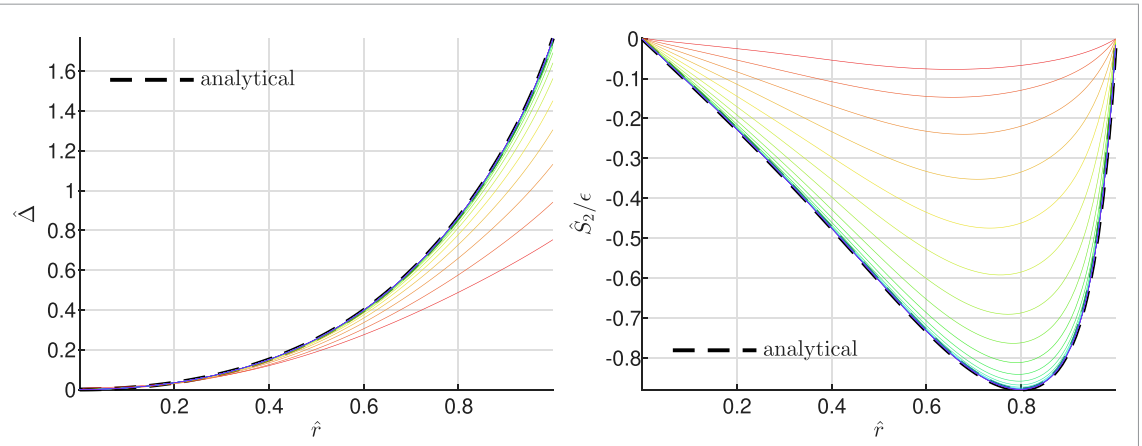


Figure 10. Normalized shift (left) and elongation (right). Colored lines are the numerical solutions, with aspect ratio of figure 9 while the analytical predictions are in dashed black. The elongation is divided by ϵ to compare with the NLO prediction $\hat{S}_{2,1}$.

5. Conclusion

In this work, a next-to-leading-order asymptotic expansion in inverse aspect ratio for pressure-anisotropic, rotating tokamak equilibria was developed and formulated so that it maps directly onto the

fixed-boundary numerical problem used for verification. We implemented a new 'exact' fixed-boundary equilibrium solver that extends the formulation of Lao *et al* (1981) to include rotation and pressure anisotropy. The code uses high-order B-spline FEs to discretize the extended Grad-Shafranov residuals, with the Jacobian computed symbolically enabling a Newton method to be used. The numerical implementation was validated against an analytically tractable test case. Implementation of different distribution functions adapted to any kinetic species is straightforward, requiring only the analytical expression of the normalized parallel pressure as a function of $(\hat{r},\hat{R},\hat{B})$. The extension to the full treatment of quasineutrality and different species, relevant for the study of heavy impurities, is also possible without large modifications to the code. The direct comparison between the asymptotic expansion and the numerical solutions yields three principal results relevant to experiment and modeling: (i) the NLO correction to the Shafranov shift significantly improves agreement with the full solution for experimentally relevant aspect ratios and shaped cross sections; (ii) the NLO correction to elongation only improves the approximation at very large aspect ratios ($A \gtrsim 10$) and only the LO prediction should be used for relevant aspect ratios, which means that the coupling with neighboring and other shaping harmonics can be neglected; (iii) for the strongly perpendicular anisotropic regime anticipated to produce strong shaping in Madden and Hastie (1994) via pressure localization, the drive is found to only weakly affect the shaping for the tested parameter regimes. This framework further enables analytical investigation of the physics of tight-aspect ratio, high-β_p, highly shaped plasmas, going beyond the perturbative estimates used in the current work. The new ('exact') code will serve to benchmark the rotation/anisotropy module of the free-boundary code LIUQE (Moret *et al* 2015) in the fixed boundary limit, and, together with the ideal MHD stability solver VENUS-MHD, will allow quantitative assessment of how the stability problem is affected by effects not captured at the order of the asymptotic expansion.

Data availability statement

The code and data supporting the findings of this study are publicly available at: https://github.com/GitGVP/EQUIL.

Appendix A. Moment equations

In what follows, we denote the degrees of freedom of the problem as F_m, such that $R(\rho,\theta) = f_R(F_m(\rho),\rho,\theta)$ and $Z(\rho,\theta) = f_Z(F_m(\rho),\rho,\theta)$ with generic independent variables (ρ,θ) spanning the poloidal plane. We call each choice of a set of F_m as different representations. One can then obtain the Euler–Lagrange (EL) equations for this representation:

$$\mathrm{EL}(F_m) = \left\langle \mathrm{EL}(R)\frac{\partial R}{\partial F_m} + \mathrm{EL}(Z)\frac{\partial Z}{\partial F_m} \right\rangle = \left\langle RF_\psi \left(-Z_\theta \frac{\partial R}{\partial F_m} + R_\theta \frac{\partial Z}{\partial F_m} \right) \right\rangle \tag{A1}$$

where EL denotes the corresponding EL equation. This is obtained from the action presented in Lao *et al* (1981), with Lagrangian density $\mathcal{L} = B_p^2/(2\mu_0) - B_\phi^2/(2\mu_0) - p$, with the first term a kinetic energy for ψ and the rest a potential energy (hence the sign). For the representation of Fitzpatrick (2024), used for the inverse aspect ratio expansion, extended to up-down asymmetric cases, the equations are:

$$\mathrm{EL}(\Delta) = \left\langle R\frac{\partial Z}{\partial \omega}F_\psi \right\rangle \tag{A2}$$

$$\mathrm{EL}(S_m) = \left\langle RF_\psi \left(\frac{\partial Z}{\partial \omega}\cos((m-1)\omega) + \frac{\partial R}{\partial \omega}\sin((m-1)\omega) \right) \right\rangle \tag{A3}$$

$$\mathrm{EL}(V_m) = \left\langle RF_\psi \left(\frac{\partial Z}{\partial \omega}\sin((m-1)\omega) + \frac{\partial R}{\partial \omega}\cos((m-1)\omega) \right) \right\rangle. \tag{A4}$$

Appendix B. Higher order expansion for shearless equilibria

Here we set $q = 1$ so that all operators $\mathcal{L}_{\mathrm{dia}}, \mathcal{L}_\Delta, \mathcal{L}_m$ have analytical inverses, and $\beta(\hat{r}) = \beta_0(1-\hat{r}^2)$ which makes all forcings simple functions of $\hat{r}$ that can be integrated explicitly. We solve for $\hat{S}_2, \hat{S}_3$ only, which is justified only for cross-sections which have small driven higher order shaping $\hat{S}^{\mathrm{BC}}_{m\geq 4} \ll 1$. Here we

choose the isotropic rotating distribution function, but the same method applies for any of the presented distribution functions. The following expressions are obtained automatically from CAS, starting with the diamagnetism profile:

$$\begin{aligned} t_2(\hat{r}) = (\beta_0 - 1)\hat{r}^2 + \epsilon^2\Big(&- 2\left(\hat{S}_2^{\mathrm{BC}}\right)^2\hat{r}^2 - \frac{1}{32}\hat{r}^4\Big(16\beta_0^2\left(3\left(\mathcal{M}_0^2\right)^2 + 6\mathcal{M}_0^2 + 4\right) \\ &+ 8\beta_0\left(-2\left(\mathcal{M}_0^2\right)^2 + \mathcal{M}_0^2 + 7\right) + 192\left(\hat{S}_3^{\mathrm{BC}}\right)^2 - 3\Big)\Big) \\ &+ \frac{1}{48}\hat{S}_2^{\mathrm{BC}}\hat{r}^2\epsilon^3\Big(48\beta_0^2\left(\mathcal{M}_0^2\right)^2 + 96\beta_0^2\mathcal{M}_0^2 + 48\beta_0^2 - 32\beta_0\left(\mathcal{M}_0^2\right)^2 - 64\beta_0\mathcal{M}_0^2 \\ &+ 24\hat{r}^2\Big(-12\beta_0^2\left(\mathcal{M}_0^2 + 1\right)^2 + 2\beta_0\left(2\left(\mathcal{M}_0^2\right)^2 + \mathcal{M}_0^2 - 3\right) \\ &+ 3\hat{S}_3^{\mathrm{BC}}\left(12\beta_0\left(\mathcal{M}_0^2 + 1\right) + 5\right) - 3\Big) \\ &- 48\hat{S}_3^{\mathrm{BC}}\left(8\beta_0\left(\mathcal{M}_0^2 + 1\right) + 1\right) + 9\Big) + \mathcal{O}(\epsilon)^4 \end{aligned} \tag{B1}$$

where we see the pressure-driven diamagnetism and the term coming from the q profile at LO, a vanishing 1st order (hence order 2 convergence to the LO in simulations), and more complicated combinations at higher order, with numerical coefficients and powers of $(\beta_0, \mathcal{M}_0^2, \hat{S}_2^{\mathrm{BC}}, \hat{S}_3^{\mathrm{BC}})$ that are growing with order ϵ^k, suggesting that the series is divergent in some parameter ranges and therefore only asymptotic. The other profiles lead to the same conclusions: for the elongation (truncated at order 3 for clarity):

$$\begin{aligned} \hat{S}_2(\hat{r}) = \hat{S}_2^{\mathrm{BC}}\hat{r} + &\frac{1}{192}\hat{r}\left(\hat{r}^2 - 1\right)\epsilon\Big(48\beta_0^2\left(\mathcal{M}_0^2 + 1\right)^2 - 32\beta_0\mathcal{M}_0^2\left(\mathcal{M}_0^2 + 2\right) \\ &- 48\hat{S}_3^{\mathrm{BC}}\left(8\beta_0\left(\mathcal{M}_0^2 + 1\right) + 1\right) + 9\Big) \\ &+ \frac{1}{24}\hat{S}_2^{\mathrm{BC}}\hat{r}\left(\hat{r}^2 - 1\right)\epsilon^2\Big(12\beta_0^2\left(\mathcal{M}_0^2 + 1\right)^2 - \beta_0\left(8\left(\mathcal{M}_0^2\right)^2 + 35\mathcal{M}_0^2 + 27\right) \\ &+ 312\left(\hat{S}_3^{\mathrm{BC}}\right)^2 - 6\hat{S}_3^{\mathrm{BC}}\left(20\beta_0\left(\mathcal{M}_0^2 + 1\right) + 1\right) - 3\Big) + \mathcal{O}(\epsilon)^3 \end{aligned} \tag{B2}$$

where it is manifest that we use the LO to satisfy the boundary conditions $\hat{S}_2(1) = \hat{S}_2^{\mathrm{BC}}$, as all higher order contributions have radial dependence as $\hat{r}(\hat{r}^2 - 1)$. Similar expressions are obtained for $\hat{\Delta}$ and $\hat{P}$.

Appendix C. Near axis forces with strongly trapped bi-Maxwellian

The modified bi-Maxwellian presented in equation (2.16) with choice $B_c = \min_\omega B$ corresponds to a standard bi-Maxwellian evaluated at the field minimum, as stated in Madden and Hastie (1994). We first remark that with $\hat{B} = \hat{B}_0 + \hat{B}_1(\omega)\hat{r} + \mathcal{O}(\hat{r})^2$, with $\hat{B}_0 = g_0/R_0$, which is valid for any ϵ, then $\min_\omega B \propto r \sim \sqrt{\psi}$ which breaks the assumption that all profiles (free functions) should be analytical functions of their arguments. One can prove that such a distribution function leads to unbalanced forces by expanding both $\boldsymbol{F}\cdot\nabla\phi = 0$ and $\boldsymbol{F}\cdot\nabla\psi = 0$ order by order in $\hat{r}$, without ever invoking the aspect ratio expansion, but this leads to unnecessarily complicated algebra. We choose instead to use the same method as in the previous section, appendix B, i.e. assume a parabolic pressure profile $\beta_t(\hat{r}) = \beta_0(1 - \hat{r}^2)$ and a constant q profile $q = 1$, constant anisotropy $T_\perp/T_\parallel = A_0 = \mathrm{cst}$, expand the equations in ϵ and obtain for the shift:

$$\begin{aligned} \hat{\Delta}(\hat{r}) = \frac{1}{8}\hat{r}^2\left(2\left(A_0 + 1\right)\beta_0 + 1\right) + \epsilon\Big(&\frac{1}{8}\hat{S}_2^{\mathrm{BC}}\hat{r}^2\left(6\left(A_0 + 1\right)\beta_0 - 32\hat{S}_3^{\mathrm{BC}} + 1\right) \\ &- \frac{1}{15}\left(2A_0^2 - A_0 - 1\right)\beta_0\hat{r}\left(3\hat{r}^2 - 5\right)\Big) + \mathcal{O}(\epsilon)^2 \end{aligned} \tag{C1}$$

which is linear in $\hat{r}$ with the term $-\beta_0\epsilon\hat{r}(A_0 - 1)(2A_0 + 1)/3$, inconsistent with equation (3.1). This linear term vanishes for $A_0 = 1$ which is the isotropic case. In the numerical simulations, this is seen as converged solutions with $\hat{\Delta}'(0) \neq 0$ that do not represent valid magnetic equilibria.

Appendix D. Expression for common figures of merit

Here we explicit formulas for figures of merit with the LIUQE convention (Moret *et al* 2015), starting from the elongation and the triangularity

$$\kappa(\hat{r}) = \frac{\max_\omega Z(\hat{r},\omega) - \min_\omega Z(\hat{r},\omega)}{\max_\omega R(\hat{r},\omega) - \min_\omega R(\hat{r},\omega)}$$

and

$$\delta(\hat{r}) = \frac{(\max_\omega R(\hat{r},\omega) + \min_\omega R(\hat{r},\omega)) - 2R(\hat{r}, \operatorname{argmin}_\omega (Z(\hat{r},\omega)))}{(\max_\omega R(\hat{r},\omega) - \min_\omega R(\hat{r},\omega))}$$

which have the advantage to be parametrization invariant quantities but these vary in our ϵ scans shown in e.g. figure 3. Typical TCV values are $\kappa \in [1;2.5]$, $\delta \in [-0.4;0.4]$ at the plasma boundary $\hat{r} = 1$. For the normalization of the figures of merit, we use:

$$W_N = \frac{\mu_0}{4\pi}\pi R_0^2 I_p^2 = \frac{\mu_0}{4\pi}\pi R_0^2 \left(\int j_\phi \, \mathrm{d}S\right)^2.$$

The poloidal beta and internal inductance are then given by:

$$\beta_p = \frac{1}{W_N}\int p \mathrm{d}V, \qquad \ell_i = \frac{1}{W_N}\int \frac{B_p^2}{2\mu_0}\mathrm{d}V$$

with typical values: $\beta_p \leqslant 2, \ell_i \approx 1$. For the anisotropic and/or rotating cases, we use the following generalizations:

$$\beta_{p,\parallel} = \frac{1}{W_N}\int p_\parallel \mathrm{d}V, \quad \beta_{p,\perp} = \frac{1}{W_N}\int p_\perp \mathrm{d}V, \quad w_\phi = \frac{1}{W_N}\int \frac{1}{2}\rho (R\Omega)^2 \mathrm{d}V.$$

Computing these quantities more explicitly in our coordinates, the (isotropic) pressure integral is:

$$W_k = \frac{3}{2}\int p \mathrm{d}V = 2\pi\epsilon^4 \frac{R_0^3 B_0^2}{\mu_0}\int_0^1 \mathrm{d}\hat{r}\beta(\hat{r})\int_0^{2\pi}\mathrm{d}\omega\hat{J}$$

where one factor of ϵ^2 comes from geometrical factors while another ϵ^2 comes the substitution $\beta \to \epsilon^2\beta$ in section 2.1. Similar computations hold for the anisotropic and rotation case. The I_p integral yields:

$$W_N = \frac{1}{4}\frac{R_0^3 B_0^2}{\mu_0}\left(\epsilon^2 \frac{T(1)}{q(1)}\int_0^{2\pi}\mathrm{d}\omega \frac{g_{\omega\omega}}{\hat{J}}\bigg|_{\hat{r}=1}\right)^2$$

and the poloidal field energy:

$$W_p = \pi\epsilon^2 \frac{R_0^3 B_0^2}{\mu_0}\int_0^1 \mathrm{d}\hat{r} f(\hat{r})^2 \int_0^{2\pi}\mathrm{d}\omega \frac{g_{\omega\omega}}{\hat{J}}$$

Then $\beta_p = (2/3)W_k/W_N$ and $\ell_i = W_p/W_N$. The leading order poloidal beta with this definition and a parabolic pressure profile $\beta(\hat{r}) = \beta_0(1-\hat{r}^2)$ gives $\beta_p = \beta_0 q(\hat{r}=1)^2$, while for a constant q the leading order internal inductance is $\ell_i = 1$.

Appendix E. Up-down symmetric Solov'ev solution and shaping coefficients extraction

In this appendix, we first outline the chosen form of rotating Solov'ev solution, followed by the extraction of the shaping coefficients given a flux map $\psi(R,Z)$, which is a standard output of other equilibrium codes.

E.1. Rotating up-down symmetric Solov'ev equilibrium

Assuming the free flux functions to be constants:

$$T\frac{\mathrm{d}T}{\mathrm{d}\psi} = C_T, \quad \frac{\mathrm{d}P}{\mathrm{d}\psi} = C_P, \quad \mathcal{M} = \mathcal{M}_0$$

leads to a linear PDE for which a family of analytical solutions to the Grad-Shafranov equation is given by Throumoulopoulos and Pantis (1989):

$$\psi(R,Z) = \sum_{n=0}^{N-1} \alpha_{n+1} R^2 \sum_{m=0}^{n} \frac{(-1)^m \left(\frac{R}{2}\right)^{2(n-m)} Z^{2m}}{(n-m)!\,(n-m+1)!\,(2m)!} - \frac{C_T Z^2}{2} - \frac{C_P R^4}{8} Q(R), \tag{E1}$$

where α_n, $n \leqslant N-1$, are numerical coefficients determined by the boundary conditions on ψ, and $Q(R) = \frac{2R_0^4}{R^4 \mathcal{M}_0^4}\left[\exp\left(\frac{\mathcal{M}_0^2 R^2}{R_0^2}\right) - \left(1 + \frac{\mathcal{M}_0^2 R^2}{R_0^2}\right)\right]$. It should be noted that the solution in equation (E1) is expressed specifically for up-down symmetric equilibria. In practice, boundary conditions are enforced at a finite set of N points, $\{(\bar{R}_k, \bar{Z}_k) \mid k = 0, \ldots, N-1\}$, such that

$$\psi\left(\bar{R}_0, \bar{Z}_0\right) \overset{!}{=} \psi\left(\bar{R}_1, \bar{Z}_1\right) \overset{!}{=} \cdots \overset{!}{=} \psi\left(\bar{R}_{N-1}, \bar{Z}_{N-1}\right)$$

which fully determine the coefficients α_{n+1}, $n \in \{0, \ldots, N-1\}$.

E.2. Extraction of shaping harmonics from the poloidal flux map

The flux surface profiles resulting from a given equilibrium can be obtained by expressing the cylindrical coordinates R and Z in the expanded (r,ω) system, as defined in equation (2.8), through integration of the function $X(r,\omega) := R(r,\omega) - \mathrm{i}Z(r,\omega)$. Namely :

$$\Delta(r) = \frac{1}{2\pi}\int_0^{2\pi} \mathrm{d}\omega X(r,\omega), \tag{E2}$$

$$S_m(r) = \frac{1}{2\pi}\int_0^{2\pi} \mathrm{d}\omega X(r,\omega)\, \mathrm{e}^{-\mathrm{i}(m-1)\omega}. \tag{E3}$$

In order to construct the (r,ω) system, one must first rely on the expressions for $R(\rho_\psi,\theta)$ and $Z(\rho_\psi,\theta)$ in a general flux coordinate system (ρ_ψ,θ). This is achieved by solving the following algebraic non-linear equation

$$\psi\left(R_0 - a(\rho_\psi,\theta)\cos(\theta),\ a(\rho_\psi,\theta)\sin(\theta)\right) = \psi_A - \rho_\psi^2(\psi_A - \psi_B)$$

for $a(\rho_\psi,\theta)$ (chosen as the smallest positive solution), here $\psi_A = \psi(R_0,0)$ and ψ_B is the value of the flux at the plasma boundary. ρ_ψ is the square root of the normalized poloidal flux, but other flux coordinates would work as well. This equation must be discretized on $\rho_\psi \in [0;1]$, $\theta \in [0;2\pi)$. The maps $R(\rho_\psi,\theta), Z(\rho_\psi,\theta)$ are not in the form of equation (2.8) as the Fourier cosine harmonics of R will generally differ to the sine harmonics of Z. Consequently, we express the geometrical angle θ as a function of the angle ω via:

$$\theta(\rho_\psi,\omega) = \omega + \sum_{k=0}^{D-1} c_k(\rho_\psi)\sin\left[(k+1)\omega\right],$$

where D denotes the chosen number of sine modes and the ρ_ψ dependence is parametric. The coefficients $c_k(\rho_\psi)$ have to be found by imposing:

$$\int_0^{2\pi} \mathrm{d}\omega X(\rho_\psi, \theta(\rho_\psi,\omega))\, \mathrm{e}^{\mathrm{i}(1+s)\omega} = 0, \quad \forall s \in \mathbb{N}^*, \tag{E4}$$

and requires $D \geqslant n_{\max}$, such that equation (E4) describes as many equations as unknowns. This system of non-linear algebraic equations is solved using a Gauss–Newton method. Since ρ_ψ is a general flux coordinate, we compute the radial coordinate r by making use of the Jacobian gauge equation (2.6) with the Jacobian of the (r,ω) system expressed as $J_{r,\omega} = \frac{\partial \rho_\psi}{\partial r} J_{\rho_\psi,\omega}$. This yields

$$r(\rho_\psi) = \sqrt{\frac{R_0}{\pi}\int_0^{\rho_\psi} \mathrm{d}\bar{\rho}_\psi \int_0^{2\pi} \mathrm{d}\omega \frac{J_{\bar{\rho}_\psi,\omega}}{R^2}},$$

completing the construction needed to extract the flux surface profiles from a given flux map.

Appendix F. Kinetic closure with multiple species & quasineutrality

Let s denote a plasma species, with distribution function $f_s = f_s(\psi, \mathcal{E}, \mu, \sigma)$ that is a function of the constants of motion from equation (2.2), we have:

$$\frac{\partial}{\partial B}\left(\frac{p_{\parallel,s}}{B}\right)_{\psi,R} = -\frac{p_{\perp,s}}{B^2} - q_s n_s \frac{1}{B}\frac{\partial \Phi_1}{\partial B} \tag{F1}$$

and:

$$\frac{\partial}{\partial R}\left(\frac{p_{\parallel,s}}{B}\right)_{\psi,B} = -\frac{n_s}{B}\left(-m_s R\Omega^2 + q_s \frac{\partial \Phi_1}{\partial R}\right) \tag{F2}$$

in summing over species in the plasma and using quasineutrality, i.e. $\sum_s q_s n_s = 0$ one gets equation (2.15) with $p_\parallel = \sum_s p_{\parallel,s}$ and $\rho = \sum_s m_s n_s$. Furthermore, the bulk thermal plasma can be shown to be Maxwellian at leading order in a magnetized expansion (Abel *et al* 2013), so that their parallel pressure is given by:

$$p_{\parallel,\mathrm{th}} = p_{0,\mathrm{th}}(\psi) \exp\left(\frac{m_{\mathrm{th}} R^2 \Omega^2}{2T_{\mathrm{th}}(\psi)}\right) \exp\left(-\frac{q\Phi_1(\psi, R, B)}{T_{\mathrm{th}}(\psi)}\right).$$

The dependence in B of the potential Φ_1 comes from the anisotropic species' contribution to the quasineutrality, which can safely be neglected as long as $n_A/n_{\mathrm{th}} \ll 1$, with n_A the density of the anisotropic specie(s), and n_{th} the density of the bulk plasma. We remark that relaxing that assumption would require to solve the quasineutrality equation for the field $\Phi_1(r, R, B)$, which adds a non-linear algebraic equation to the system, and the appearance of $(\partial_r \Phi_1, \partial_B \Phi_1, \partial_R \Phi_1)$ terms in the force balance which require considerable symbolic manipulations. On the other hand, the rotation part of Φ_1 is such that there exists an effective mach number $\mathcal{M}_0^2(T_e, T_i, m_e, m_i, \Omega; \psi)$ (Graves and Wahlberg 2017) such that:

$$p_{\parallel,\mathrm{th}} = p_{0,\mathrm{th}}(\psi) \exp\left(\mathcal{M}_0^2(\psi) R^2\right)$$

i.e. with bulk ions and electrons having different temperatures. Therefore, equations (2.16) and (2.17) are valid for multi-species plasmas with the addition of a term $\beta_{\mathrm{th}}(\hat{r})$ for the static case (e.g. bi-Maxwellian), and for the fully-parallel anisotropic, rotating, we would have:

$$\Pi_\parallel(\hat{r}, \hat{R}, \hat{B}) = \left(\beta_{\mathrm{th}}(\hat{r}) + \beta_A(\hat{r})\hat{B}\right) \exp\left(\mathcal{M}_0^2(\hat{r})\hat{R}^2\right)$$

the results presented in sections 3 and 4 take $\beta_{\mathrm{th}} = 0$ to isolate the impact of anisotropy/rotation, and not to have an additional free parameter.

ORCID iDs

G Van Parys 0000-0001-8799-9555
J P Graves 0000-0002-7959-7959
A Merle 0000-0003-1831-5644
C Heiss 0009-0005-9712-0643
T Glauser 0009-0000-5549-1474

References

Abel I G, Plunk G G, Wang E, Barnes M, Cowley S C, Dorland W and Schekochihin A A 2013 Multiscale gyrokinetics for rotating tokamak plasmas: fluctuations, transport and energy flows *Rep. Prog. Phys.* **76** 116201

de Blank H J 1991 Theory of the m = 1 kink mode in toroidal plasmas *PhD Thesis* Eindhoven University of Technology

Brunetti D, Ham C J, Graves J P, Wahlberg C and Cooper W A 2020 Anisotropy and shaping effects on the stability boundaries of infernal ideal MHD modes in tokamak hybrid plasmas *Plasma Phys. Control. Fusion* **62** 115005

Bussac M N, Pellat R, Edery D and Soule J L 1975 Internal kink modes in toroidal plasmas with circular cross sections *Phys. Rev. Lett.* **35** 1638–41

Carpanese F 2021 Development of free-boundary equilibrium and transport solvers for simulation and real-time interpretation of tokamak experiments *PhD Thesis* EPFL

Connor J W and Hastie R J 1985 The effect of shaped plasma cross sections on the ideal internal kink mode *Technical Report* (Culham Laboratory Report)

Cooper W A, Hirshman S P, Merkel P, Graves J P, Kisslinger J, Wobig H F G, Narushima Y, Okamura S and Watanabe K Y 2009 Three-dimensional anisotropic pressure free boundary equilibria *Comput. Phys. Commun.* **180** 1524–33
Eriksson H G and Wahlberg C 2002 Effect of combined triangularity and ellipticity on the stability limit of the ideal internal kink mode in a tokamak *Phys. Plasmas* **9** 1606–21
Fitzgerald M, Appel L C and Hole M J 2013 Efit tokamak equilibria with toroidal flow and anisotropic pressure using the two-temperature guiding-centre plasma *Nucl. Fusion* **53** 113040
Fitzpatrick R 2024 Inverse aspect-ratio expanded tokamak equilibria *Phys. Plasmas* **31** 082505
Freidberg J P 2014 *Ideal MHD* (Cambridge University Press)
Grad H 1967 *Magneto-Fluid and Plasma Dynamics* (American Mathematical Society)
Graves J P and Wahlberg C 2017 Generalised zonal modes in stationary axisymmetric plasmas *Plasma Phys. Control. Fusion* **59** 054011
Graves J P 2004 Influence of asymmetric energetic ion distributions on sawtooth stabilization *Phys. Rev. Lett.* **92** 185003
Graves J P 2013 Toroidal drift precession and wave–particle interaction in shaped tokamaks with finite beta and neoclassical equilibrium effects *Plasma Phys. Control. Fusion* **55** 074009
Graves J P, Cooper W A, Coda S, Eriksson L-G and Johnson T (JET-EFDA Contributors) 2006 Modelling ICCD experiments for sawtooth control in JET *AIP Conf. Proc.* **871** 350–5
Greene J M, Johnson J L and Weimer K E 1971 Tokamak equilibrium *Phys. Fluids* **14** 671–83
Guazzotto L, Betti R, Manickam J and Kaye S 2004 Numerical study of tokamak equilibria with arbitrary flow *Phys. Plasmas* **11** 604–14
Iacono R, Bondeson A, Troyon F and Gruber R 1990 Axisymmetric toroidal equilibrium with flow and anisotropic pressure *Phys. Fluids B: Plasma Phys.* **2** 1794–803
Jucker M, Graves J P, Cooper G A and Cooper W A 2008 Impact of pressure anisotropy on tokamak equilibria and the toroidal magnetic precession *Plasma Phys. Control. Fusion* **50** 065009
Lao L L, Hirshman S P and Wieland R M 1981 Variational moment solutions to the Grad–Shafranov equation *Phys. Fluids* **24** 1431–40
Madden N A and Hastie R J 1994 Tokamak equilibrium with anisotropic pressure *Nucl. Fusion* **34** 519
Mikhailovskii A B 1998 *Instabilities in a Confined Plasma* 1st edn (CRC Press)
Moret J-M, Duval B P, Le H B, Coda S, Felici F and Reimerdes H 2015 Tokamak equilibrium reconstruction code LIUQE and its real time implementation *Fusion Eng. Des.* **91** 1–15
Throumoulopoulos G N and Pantis G 1989 Analytic axisymmetric magnetohydrodynamic equilibria of a plasma torus with toroidal mass flow *Phys. Fluids B: Plasma Phys.* **1** 1827–33
Wahlberg C 2004 Aspect ratio dependence of the ideal internal kink mode stability in a toroidal plasma with circular cross section *Phys. Plasmas* **11** 2119–34
Van Parys G 2026 EQUIL equilibrium code *Github* (available at: https://github.com/GitGVP/EQUIL)